Large Wind Ripples on Mars: A Record of Atmospheric Evolution

M. G. A. Lapotre[1*], R. C. Ewing[2], M. P. Lamb[1], W. W. Fischer[1], J. P. Grotzinger[1], D. M. Rubin[3], K. W. Lewis[4], M. Ballard[2], M. Day[5], S. Gupta[6], S. G. Banham[6], N. T. Bridges[7], D. J. Des Marais[8], A. A. Fraeman[1,9], J. A. Grant[10], K. E. Herkenhoff[11], D. W. Ming[12], M. A. Mischna[9], M. S. Rice[13], D. A. Sumner[14], A. R. Vasavada[9], R. A. Yingst[15].

Affiliations:

[1]Division of Geological and Planetary Science, California Institute of Technology, Pasadena, CA 91125, USA.

[2]Department of Geology and Geophysics, Texas A&M University, College Station, TX 77843, USA.

[3]Department of Earth and Planetary Sciences, UC Santa Cruz, Santa Cruz, CA 95064, USA.

[4]Department of Earth and Planetary Sciences, Johns Hopkins University, Baltimore, MD 21218, USA.

[5]Jackson School of Geosciences, University of Texas at Austin, TX 78759, USA.

[6]Department of Earth Science and Engineering, Imperial College London, London SW7 2AZ, UK.

[7]Applied Physics Laboratory, Johns Hopkins University, Laurel, MD 20723, USA.

[8]NASA Ames Research Center, Moffett Field, CA 94035, USA.

[9]Jet Propulsion Laboratory, California Institute of Technology, Pasadena, CA 91109, USA.

[10]National Air and Space Museum, Smithsonian Institution, Washington, DC 20560, USA.

[11]Astrogeology Science Center, U.S. Geological Survey, Flagstaff, AZ 86001-1698, USA.

[12]NASA Johnson Space Center, Houston, TX 77058, USA.

[13]Geology Department, Western Washington University, Bellingham, WA 98225-9080, USA.

[14]Department of Earth and Planetary Sciences, University of California, Davis, CA 95616, USA.

[15]Planetary Science Institute, Tucson, AZ 85719, USA.

*Correspondence to: mlapotre@caltech.edu

Abstract: Wind blowing over sand on Earth produces decimeter-wavelength ripples and hundred-meter- to kilometer-wavelength dunes—bedforms of two distinct size modes. Observations from the Mars Science Laboratory Curiosity rover and the Mars Reconnaissance Orbiter reveal that Mars hosts a third stable wind-driven bedform with meter-scale wavelengths. These bedforms are spatially uniform in size, and typically have asymmetric profiles with angle-of-repose lee slopes and sinuous crest lines, making them unlike terrestrial wind ripples. Rather, these structures resemble fluid-drag ripples, which on Earth include water-worked current ripples, but on Mars instead form by wind due to the higher kinematic viscosity of the low-density atmosphere. A reevaluation of the wind-deposited strata in the Burns formation (< ~3.7 Ga) identifies potential wind-drag ripple stratification formed under a thin atmosphere.

One Sentence Summary: Distinct from terrestrial wind-driven bedforms, stable meter-scale ripples on Mars likely result from fluid drag in a low-density atmosphere.

Bedforms are repeating topographic forms on a granular surface that arise because of interactions between the sediment bed, sediment transport, and fluid flow (*1*). Bedforms typically

manifest as ripples or dunes made of sand mobilized by air or water. They create spatial patterns that are recognizable on the surfaces of Venus, Earth, Mars, Titan, and comet 67P (e.g., *2, 3*), and leave stratified sedimentary deposits. Because their morphology depends on formation mechanisms (*4-6*), bedforms are a primary means to reconstruct active and ancient atmospheric and hydrologic conditions.

Wind-driven (eolian) bedforms on Earth display two distinct scales: decimeter-wavelength sand ripples, and hundred-meter- to kilometer-wavelength dunes (*4, 7*) (Fig. 1A). Grain-impact processes are thought to dominate the formation of wind ripples, whereas dune formation involves an aerodynamic instability (e.g., *6*). Orbital observations of Mars also show the superposition of two distinct scales of active bedforms (Fig. 1B and S3) (*8*). Dunes form at a similar wavelength as on Earth; however, dunes are ubiquitously mantled with bedforms 1-5 m in wavelength (hereafter referred to as large martian ripples) (*9*).

Large martian ripples were thought to have a similar origin to decimeter-wavelength eolian impact ripples on Earth, but to be larger on Mars due to differences in saltation (ballistic hopping of grains) (e.g., *6*). An implicit assumption under this hypothesis is that small wind ripples should not coexist with large martian ripples. Until recently, the spatial coexistence of three scales of bedforms could not be tested because the resolution of orbital imagery is too coarse (25-50 cm/pixel with High Resolution Imaging Experiment (HiRISE) images (*10*)) to detect decimeter-scale ripples, and rovers had not visited active dune fields – only sand sheets and coarse-grained ripples (e.g., *11, 12, 13*). Observations made by the Curiosity rover (*14*) at an active dune field (the "Bagnold Dune Field") (*15*) in Gale crater now show that large martian ripples are not simply larger versions of decimeter-scale wind ripples seen on Earth. Rather, we observe decimeter-scale ripples superimposed on larger, meter-scale ripples, which are in turn

superimposed on dunes (Fig. 1 and S2). Thus, two stable ripple-scale bedforms coexist on Mars, and are both superimposed on dunes, in contrast to the single scale of superimposed terrestrial ripples.

Mast Camera (Mastcam (*14*)) images collected by Curiosity indicate that large martian ripples have morphologies unlike eolian impact ripples. Terrestrial impact ripples have straight crestlines created by lateral grain splash (*16*), and relatively subdued profiles (*17*). In contrast, the large ripples of the Bagnold Dune Field have sinuous crest lines and asymmetric topographic profiles with distinct upwind (stoss) and downwind (lee) slope angles. Furthermore, the stoss slopes of the large ripples are mantled by small-scale ripples with a wavelength range of ~ 5-12 cm, which, based on their straight crestline, we interpret as impact ripples similar to those of Earth (Fig. 1C and D). This interpretation is consistent with recent numerical modeling which predicts that martian impact ripples should have decimeter-scale wavelengths (*18*). By contrast, the crests of the large ripples are sharp and give way downslope to angle-of-repose slip faces (slopes dipping ~30 degrees downwind; Fig. S5A) marked by the presence of grainflows – small avalanche deposits (Fig. 1D), indicating recent activity. The presence of grainfall (i.e., sand that settles out on the lee slope) and deflected impact ripples on the lee slope indicates aerodynamic influence of the large ripples contemporaneous with small-ripple migration (Fig. 1D).

We compiled a comprehensive multiscale dataset of eolian bedform wavelengths on Mars by combining remote measurements from eleven martian sites (Fig. S1; Tables S1 and S2), with rover measurements from stereo imagery in Gale crater (Fig. S5) (*7*). Our statistical analysis confirms that Mars has an additional bedform-wavelength mode, and that meter-scale ripples are absent in terrestrial eolian landscapes (Fig. 2; Table S3) (*7*).

Large martian ripples are not simply small dunes because they maintain a stable size, whereas meter-wavelength dunes, which are rare on Earth, grow as they translate downwind (*6*) (Fig. S3 vs S4). Large martian ripples mantled with impact ripples also cannot be explained as large versions of terrestrial impact ripples forming by large saltation (*18, 19*); no existing model can reproduce the coexistence and coevolution of two scales of impact ripples (e.g., *20*) (supplementary online text). Moreover, the large ripple morphology differs significantly from impact ripples. An alternative interpretation of the large ripples is that they are coarse-grained ripples (e.g., *21*). However, images from the Mars Hand Lens Imager (MAHLI (*14*)) show well-sorted large ripples up the dune's stoss slopes (Fig. 1E), with very fine to medium sand and no significant grain-size differences between the small and large ripples (Fig. 1E and F). Thus, neither the impact nor coarse-grained hypotheses readily explain the coexistence of two distinct equilibrium scales of active ripples composed of similar sediment size.

Their stable size, sinuous crests, and asymmetric profiles with avalanche faces make the large martian ripples morphologically similar to terrestrial subaqueous current ripples (Fig. S6), also called fluid-drag ripples (*22*) (supplementary online text). If the large martian ripples form aerodynamically (i.e., wind-drag ripples (*4, 23*)), then theory developed for current ripples should predict their scale once adjusted for martian conditions. Decades of flume experiments (e.g., *24-25*) have led to scaling relations for current ripples (e.g., *25-26*). Following the theoretical framework of (*25*), we cast ripple size data in terms of the dimensionless current ripple wavelength, $\lambda^* = \frac{u_*}{\nu}\lambda$ (where λ is ripple wavelength, ν is kinematic fluid viscosity, u_* is bed shear velocity, and ν / u_* is proportional to the viscous sublayer thickness (*25*)) is a function of the parameter $\mathrm{Re}_p \sqrt{\tau_*}$ (where Re_p is particle Reynolds number and τ_* is Shields stress (Fig. S7; supplementary

online text)). These dimensionless variables provide a complete description of ripple-size scaling that accounts for fluid and grain properties, and gravity. A large database of current ripple wavelengths (*25*), updated here to include results from high viscosity fluids (*24*), illustrates that

$$\lambda^* = 2453\left(\mathrm{Re}_p \sqrt{\tau_*}\right)^{1/3} \quad (1)$$

(Fig. 3). To compare the predictions of fluid-drag ripple-wavelengths to the large martian ripples, we calculated $\mathrm{Re}_p \sqrt{\tau_*}$ and λ^* for all compiled martian bedforms (*7*) (supplementary online text). Results show that wind-drag ripples on Mars are predicted to be much larger than the decimeter-scale impact ripples due to the high kinematic viscosity in Mars' low-density atmosphere; furthermore, the wavelength of the large martian ripples is consistent with fluid-drag theory (Fig. 3) across a range of elevations with different atmospheric density (Fig. S10).

Because wind-drag ripples are predicted to be smaller in thicker atmospheres, identification of these bedforms in ancient sedimentary rocks (e.g., *28*) offers the potential to reconstruct atmospheric loss and the global drying of Mars (e.g., *29*). Migration of bedforms produces cross-stratification in sedimentary rocks, which can be used to determine their original three-dimensional geometry. Based on morphology and scale, and using a kinematic model (*30*) (Fig. 4), we expect sinuous wind-drag ripples formed under present-day martian atmospheric conditions (*32*) to form decimeter-thick trough-cross-sets, grouped into larger sets formed by overall migration of the dune (supplementary online text). Large-ripple stratification should be distinct from that of compound wind dunes or coarse-grained ripples because compound dunes do not maintain a persistently stable size in the down-dip direction (e.g., Fig. S3 vs S4) and typically form thicker cross-sets, and coarse-grained ripples leave recognizable coarse grained lags. Stratification from the large ripples might also resemble that of subaqueous ripples and dunes. However, identification of distinctive

wind-ripple strata (inversely-graded, millimeter-thick continuous layers (*33*)) coexisting with both decimeter-scale cross-sets and meter-scale dune troughs would enable the definitive interpretation of an eolian origin, whereas other contextual support, such as fluvial bar sets, desiccation cracks, and soft-sediment deformation, would characterize wet environments (e.g., *28*).

Candidate wind-drag ripples were observed by the Opportunity rover at Cape St. Mary, Victoria crater, in the Burns formation (Fig. 4; supplementary online text) (*34*), and were recognized as abnormally sinuous and large eolian ripples at the time. There, repeated 10-20 cm thick trough cross-sets are bounded by meter-scale dune troughs. The morphology, scale, contextual relationship to distinctly larger bounding surfaces, and apparent high deposition rate (*34*) all support the hypothesis that this stratification was formed by wind-drag ripples. The wind-drag ripple hypothesis therefore indicates a substantially thinned martian atmosphere during deposition of the Late Noachian-Early Hesperian Burns formation (Fig. S10) (*35*). This interpretation supports models for atmospheric loss based on carbon isotope calculations (e.g., *29*). The implied paleo-hydrology does not conflict with recent observations from Gale crater (*36*) since the absolute ages of both sequences are highly uncertain, and is also consistent with centimeter-scale trough cross-strata in sulfate-rich sands in the lower Burns formation (*28*). The latter indicate shallow subaqueous flows discharged from melt or groundwater as brines of high ionic strength due to highly soluble sand grains (*26, 37, 38*), rather than sourced from meteoric precipitation under a denser atmosphere. Thus, whereas aqueous activity can be local and sourced from the subsurface (*39*), widespread shifts in wind-drag ripple size can indicate global changes in atmospheric density, and should prove an important geological indicator of the drying of Mars (Fig. S8 and S9).

References:

1. G. V. Middleton, J. B. Southard, *Mechanics of sediment movement*. (SEPM Society for Sedimentary Geology, ed. 2, 1984), pp. 401.

2. J. Grotzinger, A. Hayes, M. Lamb, S. McLennan, in *Comparative Climatology of Terrestrial Planets,* S. Mackwell, M. Bullock, J. Harder, Eds. (University of Arizona Press, 2013), pp. 439-472.

3. N. Thomas *et al.*, *Science* **347**, aaa0440 (2015).

4. I. G. Wilson, *Sedimentology* **19**, 173 (1972).

5. D. Rubin, D. McCulloch, *Sedimentary Geology* **26**, 207 (1980).

6. J. F. Kok, E. J. Parteli, T. I. Michaels, D. B. Karam, *Reports on Progress in Physics* **75**, 106901 (2012).

7. Materials and methods are available as supplementary materials on Science Online.

8. N. T. Bridges *et al.*, *Geology* **40**, 31 (2012).

9. N. Bridges *et al.*, *Geophysical Research Letters* **34**, (2007).

10. A. S. McEwen *et al.*, *Journal of Geophysical Research: Planets (1991-2012)* **112**, (2007).

11. R. Sullivan *et al.*, *Nature* **436**, 58 (2005).

12. D. J. Jerolmack, D. Mohrig, J. P. Grotzinger, D. A. Fike, W. A. Watters, *Journal of Geophysical Research: Planets (1991-2012)* **111**, (2006).

13. D. F. Blake *et al.*, *Science* **341**, 1239505 (2013).

14. J. P. Grotzinger *et al.*, *Space Science Reviews* **170**, 5 (2012).

15. S. Silvestro *et al.*, *Geology* **41**, 483 (2013).

16. D. M. Rubin, *Earth-Science Reviews* **113**, 176 (2012).

17. B. Werner, P. Haff, R. Livi, R. Anderson, *Geology* **14**, 743 (1986).

18. H. Yizhaq, J. Kok, I. Katra, *Icarus* **230**, 143 (2014).

19. O. Duran, P. Claudin, B. Andreotti, *Proceedings of the National Academy of Sciences* **111**, 15665 (2014).

20. B. Andreotti, P. Claudin, O. Pouliquen, *Physical review letters* **96**, 028001 (2006).

21. S. De Silva, M. Spagnuolo, N. Bridges, J. Zimbelman, *Geological Society of America Bulletin* **125**, 1912 (2013).

22. J. B. Southard, L. A. Boguchwal, *Journal of Sedimentary Research* **60**, 658 (1990).

23. R. Bagnold, *The physics of blown sand and desert dunes*. (Methuen and Co., London, 1941), vol. 10, pp. 265.

24. Grazer, R. A. (1982), *Experimental study of current ripples using medium silt*, 131 pp., Massachusetts Institute of Technology.

25. M. S. Yalin, *Journal of Hydraulic Engineering* **111**, 1148 (1985).

26. M. P. Lamb, J. P. Grotzinger, J. B. Southard, N. J. Tosca, *Sedimentary Geology of Mars* **102**, 139 (2012).

27. R. D. Lorenz, N. T. Bridges, A. A. Rosenthal, E. Donkor, *Icarus* **230**, 77 (2014).

28. J. P. Grotzinger *et al.*, *Earth and Planetary Science Letters* **240**, 11 (2005).

29. R. Hu, D. M. Kass, B. L. Ehlmann, Y. L. Yung, *Nature communications* **6**, 10003 (2015).

30. D. M. Rubin, C. L. Carter, "Bedforms 4.0: MATLAB code for simulating bedforms and cross-bedding" *2331-1258* (U.S. Geological Survey Open-File Report, 2005).

31. J. Bell *et al.*, *Journal of Geophysical Research: Planets* **108**, (2003).

32. P. Withers, M. D. Smith, *Icarus* **185**, 133 (2006).

33. R. E. Hunter, *Sedimentology* **24**, 361 (1977).

34. A. Hayes *et al.*, *Journal of Geophysical Research: Planets (1991-2012)* **116**, (2011).

35. R. Arvidson *et al.*, *Journal of Geophysical Research: Planets* **111**, (2006).

36. P. Mahaffy *et al.*, *Science* **347**, 412 (2015).

37. N. J. Tosca *et al.*, *Earth and Planetary Science Letters* **240**, 122 (2005).

38. N. J. Tosca, S. M. McLennan, M. P. Lamb, J. P. Grotzinger, *Journal of Geophysical Research: Planets (1991-2012)* **116**, (2011).

39. L. Ojha *et al.*, *Nature Geoscience* **8**, 829 (2015).

40. B. W. Silverman, *Journal of the Royal Statistical Society. Series B (Methodological)*, 97 (1981).

41. N. Lancaster, *Geology* **16**, 972 (1988).

42. R. S. Anderson, *Earth-Science Reviews* **29**, 77 (1990).

43. R. C. Ewing, G. A. Kocurek, *Sedimentology* **57**, 1199 (2010).

44. R. C. Ewing, G. Kocurek, L. W. Lake, *Earth Surface Processes and Landforms* **31**, 1176 (2006).

45. M. Chojnacki, D. M. Burr, J. E. Moersch, T. I. Michaels, *Journal of Geophysical Research: Planets* **116**, (2011).

46. M. Chojnacki *et al.*, *Icarus* **251**, 275 (2015).

47. S. Silvestro, L. Fenton, D. Vaz, N. Bridges, G. Ori, *Geophysical Research Letters* **37**, (2010).

48. N. Bridges *et al.*, *Nature* **485**, 339 (2012).

49. F. Ayoub *et al.*, *Nature communications* **5**, 5096 (2014).

50. ArcGIS software, www.arcgis.com.

51. R. C. Ewing, A.-P. B. Peyret, G. Kocurek, M. Bourke, *Journal of Geophysical Research: Planets (1991-2012)* **115**, (2010).

52. M. Balme, D. C. Berman, M. C. Bourke, J. R. Zimbelman, *Geomorphology* **101**, 703 (2008).

53. M. P. Almeida, E. J. Parteli, J. S. Andrade, H. J. Herrmann, *Proceedings of the National Academy of Sciences* **105**, 6222 (2008).

54. J. R. Zimbelman, *Geomorphology* **121**, 22 (2010).

55. P. E. Geissler, *Journal of Geophysical Research: Planets* **119**, 2583 (2014).

56. N. Bridges, P. Geissler, S. Silvestro, M. Banks, *Aeolian Research* **9**, 133 (2013).

57. D. A. Vaz, S. Silvestro, *Icarus* **230**, 151 (2014).

58. R. P. Sharp, *The Journal of Geology* **71**, 617 (1963).

59. N. Bridges, M. Spagnuolo, S. de Silva, J. Zimbelman, E. Neely, *Aeolian Research* **17**, 49 (2015).

60. R. Sullivan *et al.*, *Journal of Geophysical Research: Planets (1991-2012)* **113**, (2008).

61. M. Sweet, J. Nielson, K. Havholm, J. Farrelley, *Sedimentology* **35**, 939 (1988).

62. R. Bagnold, *Geographical journal* **89**, 409 (1937).

63. W. Chepil, *Soil Science* **60**, 397 (1945).

64. J. D. Iversen, K. R. Rasmussen, *Sedimentology* **46**, 723 (1999).

65. B. Li, C. McKenna Neuman, *Geophysical Research Letters* **39**, 11 (2012).

66. J. F. Kok, *Geophysical Research Letters* **37**, 6 (2010).

67. L. A. Soderblom *et al.*, *Science* **306**, 1723 (2004).

68. A. Seiff, D. B. Kirk, *Journal of Geophysical Research* **82**, 4364 (1977).

69. J. R. Barton, P.-n. Lin (1955), *A Study of the Sediment Transport in Alluvial Channels*. Report 55, JRB2, Civil Engineering Department, Colorado A and M College.

70. V. A. Vanoni, N. H. Brooks (1957), *Laboratory studies of the roughness and suspended load of alluvial streams*, 121 pp., California Institute of Technology Sedimentation Laboratory).

71. V. A. Vanoni, L.-S. Hwang, *Journal of the Hydraulics Division* **93**, 121 (1967).

72. L. J. D. Alexander (1980), *On the geometry of ripples generated by unidirectional open channel flows*, 107 pp., National Library of Canada.

73. J.-I. Van den Berg, A. Van Gelder, *Alluvial Sedimentation (Special Publication 17 of the International Association of Sedimentologists)* **66**, 11 (2009).

74. M. S. Yalin, *Mechanics of sediment transport*, 298 pp. (Pergamon Press, 1977).

75. A. J. Raudkivi, *Journal of Hydraulic Engineering* **123**, 58 (1997).

76. M. Garcia, in *Sedimentation engineering: processes, measurements, modeling, and practice,* 1132 pp. (American Association of Civil Engineers, 2008).

77. J. B. Southard, L. A. Boguchwal, *Journal of Sedimentary Research* **60**, 680 (1990).

78. L. A. Boguchwal, J. B. Southard, *Journal of Sedimentary Research* **60**, 649 (1990).

79. J. H. Baas, *Sedimentology* **46**, 123 (1999).

80. J. Allen, *Sedimentology* **20**, 189 (1973).

81. C. Paola, L. Borgman, *Sedimentology* **38**, 553 (1991).

82. S. F. Leclair, *Sedimentology* **49**, 1157 (2002).

83. D. M. Rubin, R. E. Hunter, *Sedimentology* **29**, 121 (1982).

84. J. M. Ellwood, P. D. Evans, I. G. Wilson, *Journal of Sedimentary Research* **45**, (1975).

85. H. P. Guy, D. B. Simons, E. V. Richardson, "Summary of alluvial channel data from flume experiments, 1956-61", *2330-7102* (U.S.G.S, 1966).

86. J. Grotzinger *et al.*, *Geology* **34**, 1085 (2006).

87. J. M. Metz *et al.*, *Journal of Sedimentary Research* **79**, 247 (2009).

88. K. W. Lewis *et al.*, *Journal of Geophysical Research: Planets (1991-2012)* **113**, (2008).

89. S. W. Squyres *et al.*, *Science* **316**, 738 (2007).

Acknowledgments: We thank the MSL engineering and science teams, the Mastcam team, and Malin Space Science Systems who made the rover observations possible, and Bethany Ehlmann and Ken Edgett for insightful comments. Data presented in this paper are archived in the Planetary Data System (pds.nasa.gov), and our compilation is available in a supplementary file. Part of this research was carried out at JPL-Caltech, under a contract with NASA. Work in the UK was funded by the UK Space Agency.

Supplementary Materials:

Materials and Methods/Supplementary Text

Fig S1 – S10

Table S1 – S3

References (40-89)

Bedform-wavelength compilations (.csv file)

Summary of parameters for martian bedforms (.csv file)

Fig. 1. Eolian bedforms on Earth and Mars. (**A**) Dunes and ripples at Oceano Dunes, California, United States (35.094960 N, -120.623476 E) (**B-F**) dune in the Bagnold Dune Field, Gale crater, Mars, as shown from (**B**) HiRISE image (ESP_035917_1755) and (**C-F**) the Curiosity rover. (**C**) Mastcam mosaic (mcam05410, sol 1192) showing small and large ripples on the dune. (**D**) Mastcam image (mcam05600, sol 1221) of large ripples with superimposed small ripples. **(E)** MAHLI 25 cm-standoff image (1223MH0005550010403094C00, sol 1223), ~1 m off-frame of (D) in the direction of the dot-and-arrow. **(F)** 5 cm-standoff image (1223MH0005560010403097C00, sol 1223) of the crest of a large ripple.

Fig. 2. Distinct modes of eolian bedforms on Earth and Mars. Bedform wavelength distribution on (**A**) Earth (n = 1473), (**B**) Mars from orbit (n = 2430; shaded area below limit of detection), and (**C**) the Curiosity rover (n = 44; shaded area constrained by perspective from the ground) (*7*).

Fig. 3. Scaling of fluid-drag ripples. Dimensionless bedform wavelength as a function of particle Reynolds number, Re_p, and Shields stress, τ^*, quantities that control fluid-drag ripple size (*25*) (current ripples in blue circles, theory in black line). In contrast to martian dunes (pink squares) and small martian ripples (orange triangles), large martian ripples (red diamonds, n = 7280, measured over 36 locations globally including our measurements (*7*) and those of (27); red star indicate rover measurements at Gale crater) match fluid-drag ripple theory. Symbols are means and error bars represent standard deviations at a given measurement site; error bars are smaller than marker size where not shown.

297 **Fig. 4. Candidate wind-drag ripple stratification on Mars. (A)** Mars Exploration Rover
298 Panoramic Camera (*31*) image (P2441, sol 1212) of Cape St Mary outcrop, Victoria crater, Mars.
299 White box shows location of **(B)** decimeter-scale trough cross-strata, and **(C)** interpretation of
300 stratal features from (B). **(D)** Uninterpreted (top) and interpreted (bottom) stratification produced
301 by geometric modeling of compound bedforms (*30*). Yellow lines represent surfaces scoured by
302 dune troughs, red lines represent erosional surfaces produced by migration of wind-drag ripples,
303 and blue lines indicate wind-drag ripple cross-stratification.

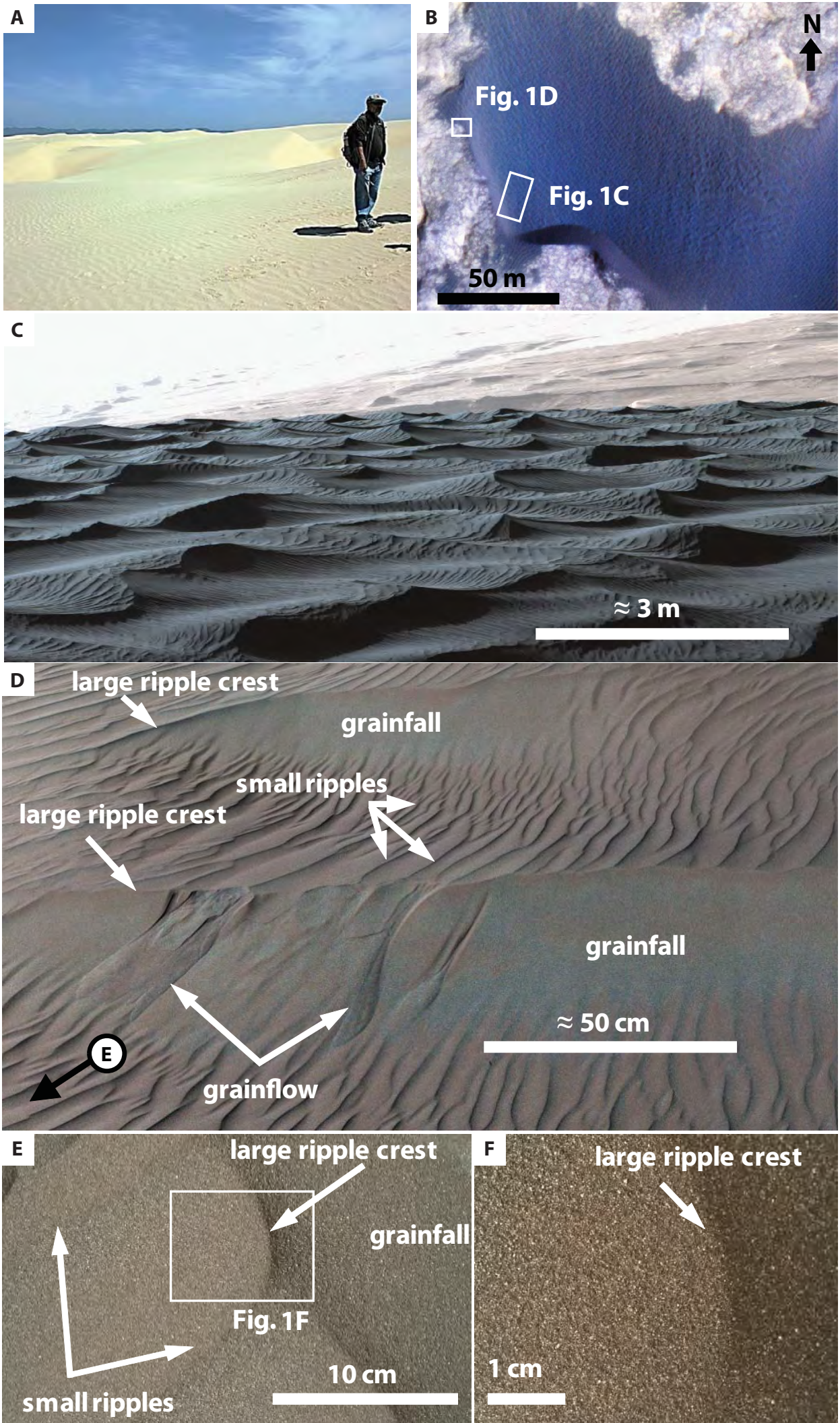
A
B
N
Fig. 1D
Fig. 1C
50 m
C
≈ 3 m
D
large ripple crest
grainfall
small ripples
large ripple crest
grainfall
≈ 50 cm
E
grainflow
E
large ripple crest
grainfall
Fig. 1F
10 cm
small ripples
F
large ripple crest
1 cm

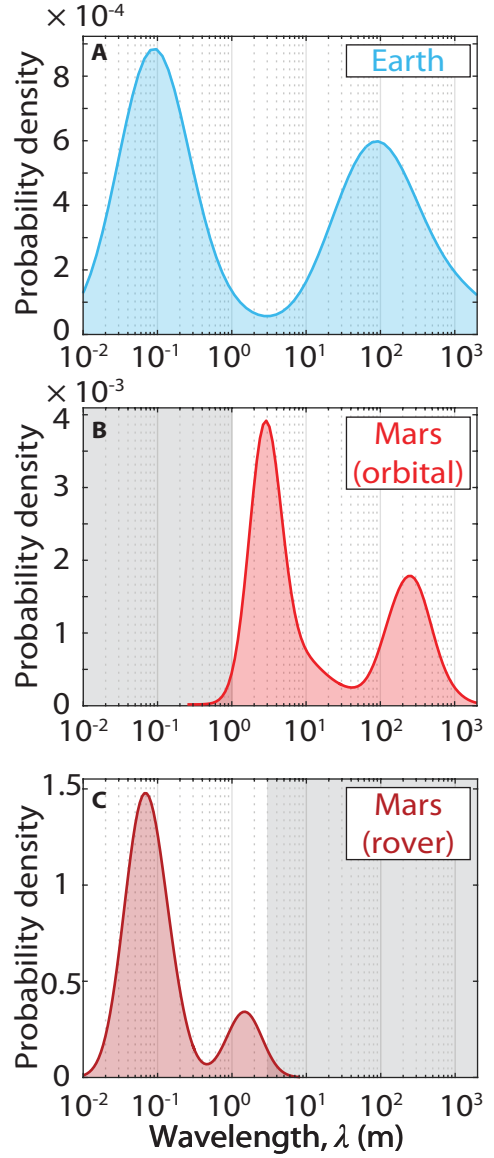
A
Earth
Probability density
× 10-4
0
2
4
6
8
10-2
10-1
100
101
102
103
B
Mars
(orbital)
Probability density
× 10-3
0
1
2
3
4
C
Mars
(rover)
Probability density
0
0.5
1
1.5
Wavelength, λ (m)

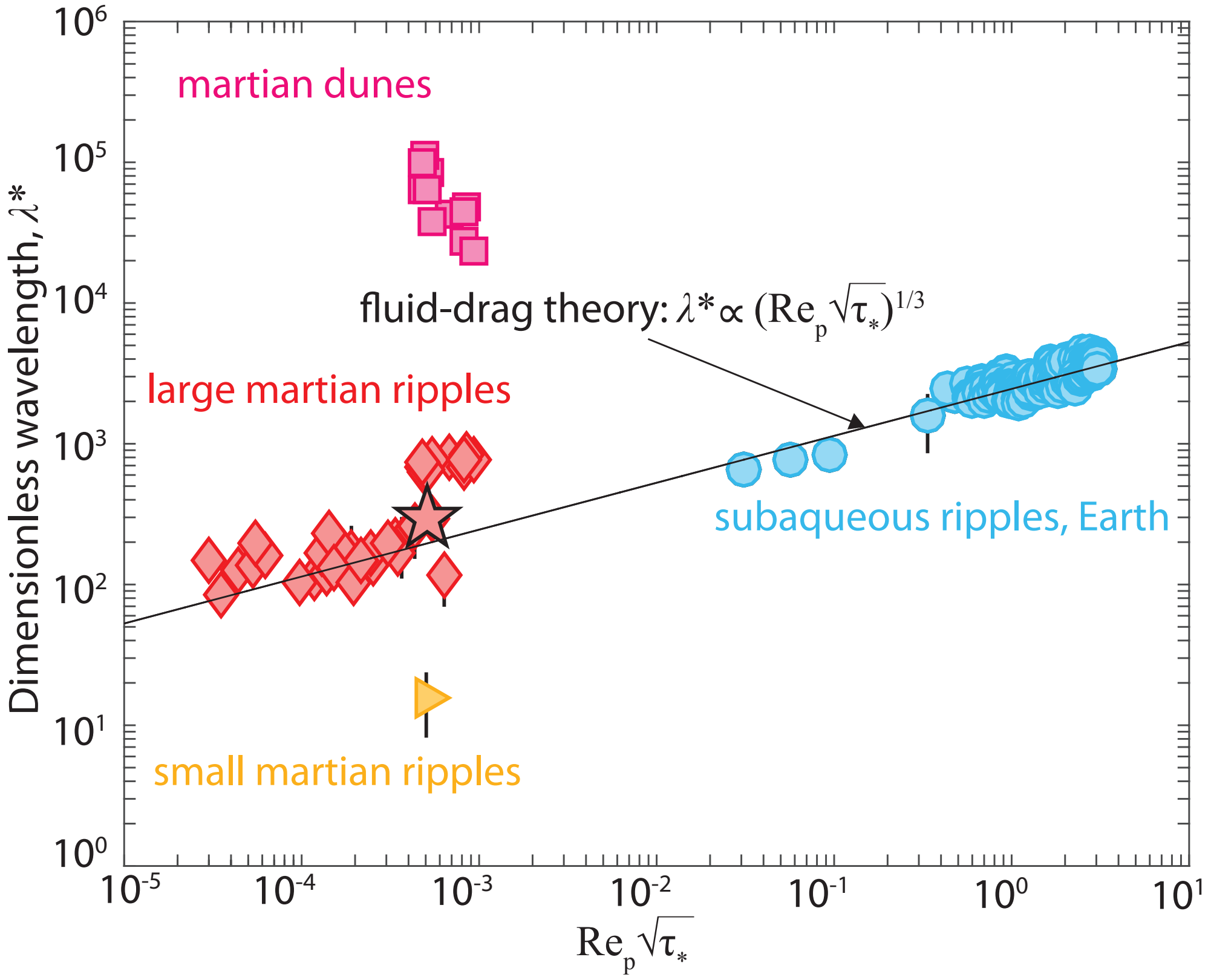
martian dunes
fluid-drag theory: $\lambda^* \propto (\mathrm{Re}_p \sqrt{\tau_*})^{1/3}$
large martian ripples
subaqueous ripples, Earth
small martian ripples
Dimensionless wavelength, λ^*
$\mathrm{Re}_p \sqrt{\tau_*}$
10^0
10^1
10^2
10^3
10^4
10^5
10^6
10^{-5}
10^{-4}
10^{-3}
10^{-2}
10^{-1}
10^0
10^1

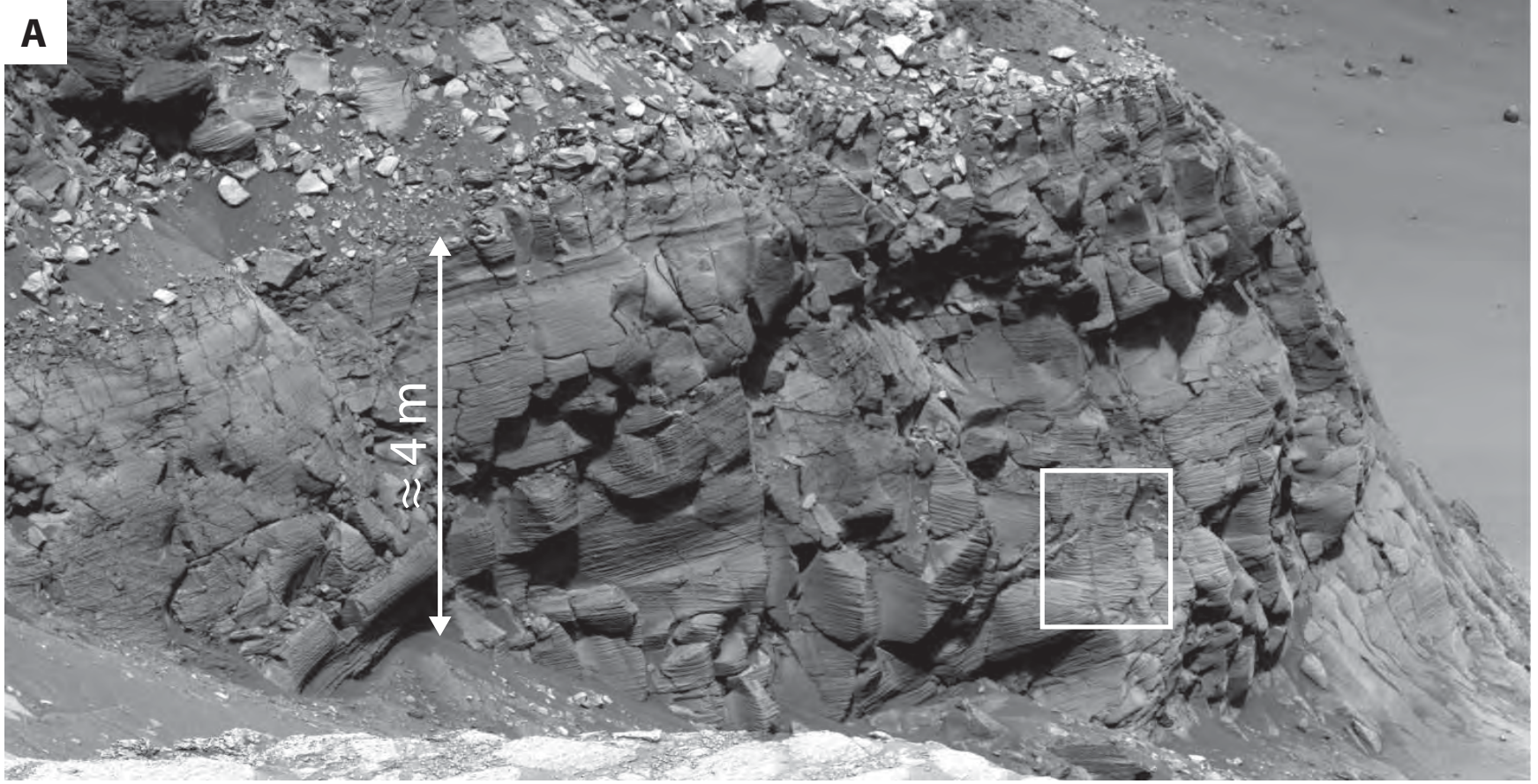
A
≈ 4 m

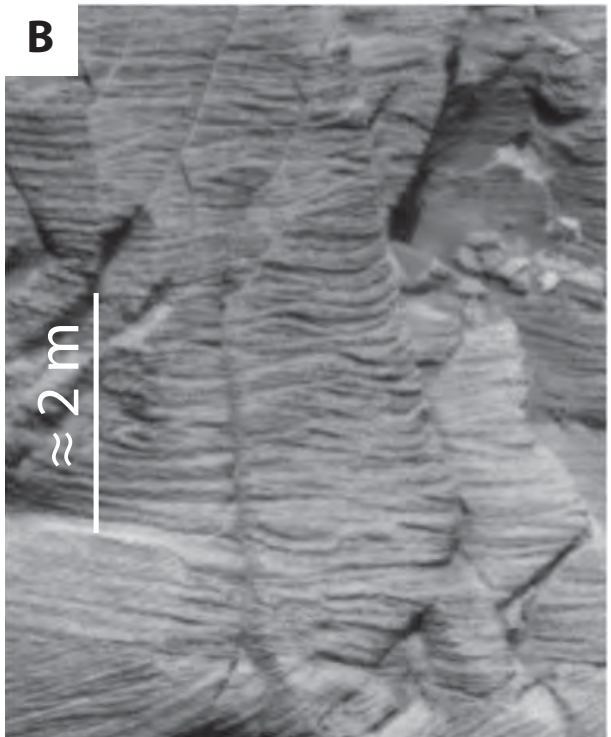
B
≈ 2 m


C

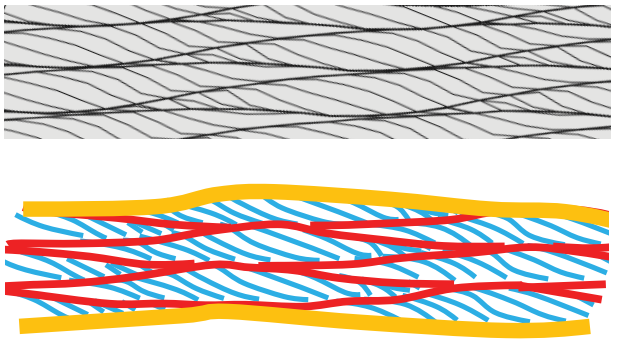
D

Supplementary Materials for

Large Wind Ripples on Mars: A Record of Atmospheric Evolution

M. G. A. Lapotre, R. C. Ewing, M. P. Lamb, W. W. Fischer, J. P. Grotzinger, D. M. Rubin, K. W. Lewis, M. Ballard, M. Day, S. Gupta, S. G. Banham, N. T. Bridges, D. J. Des Marais, A. A. Fraeman, J. A. Grant, K. E. Herkenhoff, D. W. Ming, M. A. Mischna, M. S. Rice, D. A. Sumner, A. R. Vasavada, R. A. Yingst.

correspondence to: mlapotre@caltech.edu

This PDF file includes:

Materials and Methods/Supplementary Text
Figs. S1 to S10
Tables S1 to S3
References (40-89)

Materials and Methods

S1. Bedform compilation

Wavelength data was compiled for Earth and Mars (from orbit and from the ground), and plotted as a Probability Density Function (PDF) to highlight the distribution of bedform wavelengths across all scales. The PDFs were calculated using the kernel density method (*40*), allowing for the identification of discrete modes. Because the terrestrial dataset was compiled from several studies and our own field and aerial measurements (Section S1.1), the relative heights of the ripple and dune modes do not perfectly reflect the area-weighted relative frequency of ripples and dunes. Nevertheless, the natural scale of terrestrial bedforms is well-known and is such that there are orders of magnitude more ripples than dunes per unit surface area. While we did not count the entire population of dunes, transverse eolian ridges (TARs, after the alternative spelling "Transverse Aeolian Ridges"), and ripples across the martian dune fields from orbit, a counting technique was designed to give a fair representation of the density of bedforms per unit surface area (Section S1.2), such that the relative heights of peaks in the martian orbital PDF (Fig. 2B) give a fair representation of the relative frequencies of the different bedforms. All bedforms were measured from the rover dataset, such that Fig. 2C displays relative peak heights that accurately represent the relative density of small and large ripples per unit land area.

S1.1. Earth

Wavelength data for terrestrial impact ripples and sand dunes was compiled from the published literature (*4, 41-44*), and aerial and field measurements from (i) White Sands National Monument, New Mexico, United States, (ii) Algodones Dunes, California, United States, and (iii) the Oceano Dunes, California, United States. Our dataset is available online in a "comma separated value" (.csv) file. Dune wavelength data was collected using aerial photographs and satellite images in geographic information system (GIS) software. Measurements were made using the methods of (*44*). Crestline wavelength measurements were manually digitized by creating line features perpendicular between crestlines. Ripple crestline measurements were made in the field using a tape measure stretched perpendicularly across ripple crestlines.

S1.2. Mars: Orbital measurements

The active migration of large ripples and dunes has been observed and quantified in many locations on Mars (*8, 15, 45-49*). Eleven dune fields (Fig. S1) were selected for analysis based on location at a range of latitudes and elevations on Mars (Table 1). These dune fields host a wide variety of bedform scales that include the range of orbitally recognized bedforms on Mars – large ripples, TARs, and dunes. These classifications were discerned visibly from High Resolution Imaging Science Experiment (HiRISE (*10*)) imagery (25-50 cm/pixel) based upon prior descriptions of ripples, TARs, and dunes (e.g., *48*).

Within each dune field a Region of Interest (ROI) that contained at least one dune with superimposed ripples and adjacent Transverse Aeolian Ridges (TARs) was selected. Ripple, TAR,

and dune wavelengths were analyzed from HiRISE imagery using ArcGIS software (*50*). HiRISE images have a spatial resolution of > 0.25 m, which allows bedforms ~1 m in size to be resolved. In order to obtain a reasonable statistical representation of ripple and TAR wavelengths, 100 points were randomly distributed within the ROI using the ArcGIS Create Random Points tool (Methods found at http://resources.arcgis.com/en/help/main/10.2/index.html#//00170000002r000000). Where the point fell on a ripple or TAR, which was determined visually, two wavelength measurements were made between the bedform on which the point fell and the adjacent bedform crestlines. If a point did not fall on a bedform, no measurement was made. Dune wavelength measurements were made by measuring from crest to crest for a range of dune sizes within the dune field. For each measurement made, a visual interpretation of the type of bedform was noted either as a ripple, TAR, or dune (Table 2). Ripples measured within the Bagnold Dune Field were only digitized from High Dune and Namib Dune (e.g., Fig. S2 and S3), both of which were visited by the Curiosity rover. The ROI for the Bagnold Dune Field is small because it only includes these two dunes.

The rationale for selecting random points was to reduce bias in the wavelength measurements that might artificially influence the wavelength distribution of ripples and dunes. Because most ripple wavelength variability occurs by position on the dune (*48, 51*) rather than across the dune field, a relatively small ROI was generated to ensure that a high density of wavelength measurements was distributed across a small number of dunes. Visual inspection of the random point locations confirmed that the points were distributed among the different slopes of the dune and inter-dune areas, and captured a representative sample of ripple and TAR wavelengths. Any systematic differences in ripple or TAR size is averaged out by this technique. Because only a few dunes are contained within a small ROI, the wavelengths of a range of dunes within the dune field containing the ROI, but outside of the ROI, were measured. Our measured distributions of ripple, TAR, and dune wavelengths falls within the typical range reported by previous studies, which used similar manual digitization methods and automated methods (*15, 47, 51*). Bedforms, as measured from orbital data, which cannot distinguish sub-meter bedforms, show two main modes corresponding to meter-wavelength large ripples and hundreds-of-meter wavelength dunes (Fig. 2B).

The dataset from (*27*) is added to our compilation. The elevation values reported in (*27*) were measured with respect to the Mars Reconnaissance Orbiter reference ellipsoid. These values were corrected to represent elevation with respect to the geoid for consistency with our measurements from MOLA.

S1.3. Mars: Rover measurements

The Mars Science Laboratory Curiosity rover visited the Bagnold Dune Field (Fig. S2) and imaged ripples along its traverse. Digital elevation models and orthorectified images were built from Mastcam stereo images (mcam05372, sol 1184). Topographic profiles (Fig. S5C-D) were measured across the scenes in directions perpendicular to the bedform crest lines, detrended with an order two polynomial, and averaged using a sliding window over 25 points (i.e., a 2.5-cm moving-average, Fig. S5E). Detrended, smoothed profiles were then compared to the original Mastcam frames to ensure that the measured wavelengths corresponded to actual bedforms. Results are shown in Fig. 2C. In order to be able to resolve the small ripples, the distance between the rover and the target had to be such that the maximum frame of a Mastcam image was about

~1.5 m wide, a perspective that limited the observation of large ripples and dunes from the ground. Despite these limitations, we were able to measure the wavelengths of both small and large ripples from the ground. The wavelength of all bedforms were measured within each Mastcam frame. The mode corresponding to the large ripples (Fig. 2C) strongly overlaps with the mode of large ripples as measured from orbit (Fig. 2B).

Grain sizes were estimated by measuring the intermediate axis of grains from MAHLI images of undisturbed and disturbed surfaces (i.e., grains sitting at and below the surface, respectively), based on the MAHLI pixel size corresponding to the stand-off distance of each given image. Measured grain sizes correspond to very fine (62-125 μm) to medium sand (250-500 μm). The highest resolution MAHLI image (1241MH0005720010403583C00, sol 1241) could not resolve grains below ~30 μm.

S1.4. Statistical Significance

In order to test that the terrestrial and martian bedform-wavelength distributions are statistically distinct (Fig. 2A vs. 2B and 2A vs. 2C), we conducted a series of 1000 two-sample Kolmogorov-Smirnov statistical tests for each pair of distributions. Each distribution was first subsampled to a sample size of $n = 40$ using a Metropolis-Hastings algorithm. The null hypothesis "the two samples were drawn from the same distributions" was rejected at the 95% confidence level in > 99% of cases for Earth vs. Mars orbital and Mars rover datasets, respectively.

To further characterize the statistical similarity of individual modes, we (i) subsampled the probability distributions ($n = 40$) using a Metropolis-Hastings algorithm, (ii) calculated kernel density of the subsampled distributions (*40*), and (iii) identified their modes through a local-maxima-detection routine. This procedure was completed 10 times for each dataset to build a distribution of each individual mode – small terrestrial ripples, terrestrial dunes, large martian ripples from orbit, martian dunes from orbit, small martian ripples from the ground, and large martian ripples from the ground. We then conducted a two-sample Kolmogorov-Smirnov test for each individual pair (p-values reported in Table S3). Importantly, the two highest p-values occur in comparisons of terrestrial impact ripples to small martian ripples, and of terrestrial dunes to martian dunes.

S1.5. Additional evidence in favor of the wind-drag hypothesis

Alternative hypotheses for the formation of the large martian ripples are that they are instead (i) TARs, (ii) compound dunes, (iii) coarse-grained ripples, or (iv) impact ripples.

The occurrence of a small fraction of bedforms tens of meters in wavelength (Fig. 2B) is the signature of TARs (*48, 51, 52*). TARs may form as a result of coarse-grain armoring, giant saltation trajectories, or deposition of dust transported in suspension (*52-55*), and are distinct from the large ripples in activity and morphology: (i) activity of TARs has not been detected (*46, 56*), (ii) their wavelengths are generally larger and more widely distributed (e.g., Table S2), (iii) they have symmetric topographic profiles (*54*), and (iv) they tend to have a much higher albedo than the dark, active, mafic sands. Thus, the large martian ripples are distinct from TARs.

As seen in Fig. S3, the bedforms on the stoss of the large dunes do not grow in size as they migrate up the stoss slope, unlike small compound dunes on Earth (Fig. S4). It was shown that, in

places, the wavelength of the large martian ripples may weakly increase or decrease upslope due to local variations in grain size or wind speed (*57*), although no consistent increase in height and wavelength upslope is observed, contrary to terrestrial compound dunes (*43*). Thus, the large martian ripples are distinct from compound dunes.

It is important to evaluate whether the large ripples are composed of coarse grains, which are expected to produce meter-wavelength ripples, known as megaripples or granule ripples, without the need for the wind-drag mechanism. Coarse-grained ripples on Earth typically form in grains larger than about a millimeter up to several centimeters (e.g., *12, 21, 58, 59*). Such coarse-grained ripples were observed on Mars by the Spirit rover at "El Dorado" in Gusev crater (*60*), and by the Curiosity rover at the base of the stoss slope of "High Dune" in Gale crater, as expected at the upwind margin of a dune field (*61*). The vast majority of large martian ripples, however, appear distinct from megaripples in that surface armoring from large grains does not appear to play a role in their formation. In contrast, the armored megaripples at the base of High Dune are expected because the observed ripples sit at the upwind, trailing margin of the dune field (*22, 23*) and at the change in slope from the inter-dune area to the stoss slope. The upwind margin concentrates coarse grains, and the abrupt increase in slope onto the stoss side limits the upslope transport of the coarsest grains, which results in a lag deposit. However, the armored ripples give way to well-sorted ripples of very fine to medium sand up the stoss slope toward the dune crest with the morphologic features we described for large ripples (e.g., Fig. 1D and E). Another observation that suggests that coarse grains are not responsible for the formation of the large ripples is that these bedforms cover the majority of imaged eolian dunes on Mars, which would require a mechanism that promotes the creation of lag regardless of initial grain-size distributions. In other words, the well-sorted sand that is expected to comprise the dunes, especially on dune lee faces and in the middle of a dune field far from the source area, would have a lag surface or coarse crest. Rather, as lag deposits, coarse-grained ripples should only occupy a fraction of a dune field, consistent with observations of large martian ripples juxtaposed to what are likely true coarse-grained ripples in several locations on Mars (*51*). Thus, large martian ripples are distinct from coarse-grained ripples.

The last alternative hypothesis is that the large martian ripples are impact ripples. In order to be a viable hypothesis, an impact mechanism has to (i) be able to generate meter-scale ripples, (ii) allow for two stable and active scales of impact-ripples, and (iii) reproduce the observed morphologies. While some numerical models are able to produce meter-scale impact ripples, they require wind shear velocities at or above the fluid threshold for saltation (e.g., *19*). Other modeling studies that are able to reproduce transport hysteresis, i.e., to recreate the lowered impact threshold relative to the fluid threshold, predict the formation of decimeter-scale impact ripples for shear velocities above the impact threshold but below the fluid threshold (e.g., *18*), more consistent with our observations of decimeter-scale ripples. However, none of the published models are able to reproduce two superimposed scales of active impact ripples that are stable under the same wind conditions. An experimental study (*20*) showed that equilibrated impact ripples subjected to a change in wind conditions either adjust their wavelength if the wind perturbation is large, or adjust their height. Thus, two different wavelengths could possibly be observed together, but one of the two bedform populations would have to be relict. In our case, the relict bedform would necessarily be the large ripples, otherwise, their migration would quickly rework and erase the decimeter-scale ripples. However, observations that large ripples migrate seasonally (*49*), that grainflows onlap onto small ripples, and that the small ripples do not rework the crest of large ripples (e.g., Fig. 1C), each illustrate that both scales of ripples are actively forming and migrating at the same time, under

similar wind conditions. Finally, the observed morphologies are inconsistent with an impact mechanism. Terrestrial impact ripples have straight crests due to lateral grain splash. Although large ripples migrating down the sloped flanks of martian dunes appear to have relatively straighter crests (Fig. S3), their relative two-dimensionality arises from gravity-driven, along-crest transport (*16*), and large ripples migrating up the stoss slopes of their host dunes are clearly sinuous. Furthermore, the impact mechanism does not promote the formation of angle-of-repose slip faces that extend from ripple brink to base as observed in some large martian ripples. Rather, impact ripples typically show short near-angle of repose slopes at the brink, which quickly give way downslope to lower angled slopes (*17, 58*).

S2. Calculation of $\mathrm{Re}_p\sqrt{\tau_*}$ and λ^* for the Earth and Mars eolian ripples data

In order to estimate the particle Reynolds number, $\mathrm{Re}_p = \frac{u_* D}{\nu}$ (in which u_* is the shear velocity, D is the grain size, and ν is the kinematic viscosity of the fluid), and Shields stress, $\tau_* = \frac{u_*^2}{\sqrt{RgD}}$ (in which $R = \frac{\rho_s - \rho_f}{\rho_f}$ is the submerged reduced density of the sediment, ρ_s and ρ_f are the sediment grain and fluid densities, and g is the acceleration of gravity), for the formation of bedforms on Earth and Mars, typical bed shear velocities, atmospheric densities and viscosities, and grain densities and sizes need to be constrained.

S2.1. Earth

In order to compare fluid-drag theory to observed terrestrial ripples, we use the dataset of (*4*) for grain size and ripple wavelength. We estimated shear velocity through the impact threshold shear velocity, u_{*it}^{Earth}, from grain size, D, based on a fit to field data from (*62-65*) compiled in (*6*),

$$u_{*it}^{\mathrm{Earth}} = \exp\left[4.081\times10^{-2}\log(D)^4 + 1.237\log(D)^3 + 13.98\log(D)^2 + 70.35\log(D) + 132.6\right] \quad (\mathrm{R}^2=0.9976) \quad \text{(S1)}$$

We assumed a constant atmospheric density of $\rho_f \approx 1.27$ kg/m^3, a kinematic viscosity of $\nu \approx 1.4\times10^{-5}$ m^2/s, an acceleration of gravity of $g \approx 9.81$ m/s^2, and a quartz density for the grains of $\rho_s \approx 2650$ kg/m^3.

Figure S7 illustrates that the range of wavelengths covered by terrestrial eolian ripples overlaps with the fluid-drag ripple predictions, such that wind-driven fluid-drag ripples (or "wind-drag ripples") may in fact occur on Earth (e.g. as suggested by (*4, 23*)), but are rarely recognized, possibly because their sizes should be similar to impact ripples. This overlap in scales between impact and fluid-drag eolian ripples is not expected on Mars, however.

S2.2. Mars

Most sand transport on Mars likely occurs close to the threshold bed shear velocity required to sustain saltation (*66*), a value referred to as the impact threshold velocity, u_{*it}. On Earth, the impact threshold is typically 80% of the fluid threshold value, while on Mars, the impact threshold is thought to be up to an order of magnitude lower than the fluid threshold (e.g., *6*). In order to compare the measured wavelength of martian eolian bedforms to predictions from fluid-drag theory (Fig. 3), we set the wind shear velocity to be equal to the impact threshold (i.e., $u_* = u_{*it}$), which is a function of atmospheric pressure, temperature, and grain size.

We calculated impact threshold bed shear velocity, u_{*it}^{Mars}, from grain diameter, D, surface pressure, p, and temperature, T, from the best fit relationship derived by (*66*),

$$u_{*it}^{\text{Mars}} = 5.5\times10^{-3}\left(\frac{700\text{Pa}}{p}\right)^{1/6}\left(\frac{220\text{K}}{T}\right)^{2/5} \exp\left[\left(\frac{49\mu\text{m}}{D}\right)^{3} + \left(0.29\mu\text{m}^{-1/2}\right)\sqrt{D} - \left(3.84\times10^{-3}\mu\text{m}^{-1}\right)D\right]. \quad \text{(S2)}$$

We consequently needed to estimate D, p, and T. The Opportunity rover measured sizes of mafic sand particle grains of ~ 50-150 μm at Eagle crater (*67*), while Spirit measured coarser grain sizes, up to ~ 200-300 μm at El Dorado (*11*). Grain sizes measured by Curiosity at the Namib Dune are typically ~ 200-300 μm (Fig. 1F). We thus assumed a grain size value of 200 μm. Note that the robustness of the match between the data and the scaling predictions are nearly independent of grain size. We estimated pressure from the elevation, z, of ripple wavelength measurements assuming a constant atmospheric scale height

$$p(z) = (610\text{Pa})\exp\left[\frac{-z}{11.2\text{km}}\right], \quad \text{(S3)}$$

consistent with the atmospheric entry profiles of the Mars Exploration Rover missions (*32*). We further assume an isothermal atmosphere of $T = 227$ K, a thermal profile suggested by the atmospheric entry profiles of (*32*) within the range of elevations covered by the ripple wavelengths measurements. The results are not particularly sensitive to the lapse rate we use to calculate $T(z)$; the R^2 value of the fit for $\lambda^* \propto \left(\text{Re}_p\sqrt{\tau_*}\right)^{1/3}$ when the martian large ripple data are included ranges from 0.9295 to 0.9312 with lapse rates of 0 (isothermal atmosphere, (*32*)) to -3.7 K/km, a value consistent with the Viking Lander 1 measurements (*68*).

We estimated atmospheric density at the elevation of the ripples through the ideal gas law

$$\rho_f(z) = \frac{M_{\text{CO}_2}}{r}\frac{p(z)}{T(z)}, \quad \text{(S4)}$$

where M_{CO_2} is the molar mass of carbon dioxide, and r is the ideal gas constant. We estimated the kinematic viscosity of the atmosphere at elevation z through

$$\nu(z) = \frac{\mu}{\rho_f(z)}, \tag{S5}$$

where the dynamic viscosity of the atmosphere is assumed to be constant and equal to $\mu \approx 10.8 \times 10^{-6}$ Pa.s. Finally, reduced gravity was calculated by setting $g \approx 3.78$ m/s^2 and assuming a basaltic density for the grains ($\rho_s \approx 2900$ kg/m^3).

Supplementary Text

S3. Current ripples: Scaling from flume experiments

A morphologic characteristic of subaqueous ripples is their often asymmetrical topographic profile (e.g., Fig. S6). They typically have gentle slopes upstream of a sharp ripple crest, and a near-angle-of-repose slip face downstream. They are often sinuous, and their crest-to-crest wavelength varies with flow and grain properties.

We build on the data compilation of (*25*), who compiled flume experiment data from (*69-72*), which comprise experiments with sand and glass beads of sizes ranging from 105 to 260 μm, where the fluid was either water or glycerine and water solutions. The analysis in (*25*) collapsed the ripple wavelength data into a parameter space $X_Y = 3.38\,\mathrm{Re}_p^{1/2}\,\tau_*^{1/4}$ in abscissa and $Y_Y = \dfrac{\lambda}{3.38D}\dfrac{\mathrm{Re}_p^{1/2}}{\tau_*^{1/4}}$ in ordinate, where $\mathrm{Re}_p = \dfrac{u_* D}{\nu}$ is the particle Reynolds number, and $\tau_* = \dfrac{u_*^2}{RgD}$ is the Shields stress (Section S2). Nondimensionalization allows for the same information to be recast in multiple non-unique ways, depending on the preferred dimensionless variables. Here we chose to recast the variables of X_Y and Y_Y of (*25*) into a more intuitive coordinate system following more recent work on bedform stability (*22*, *26, 73*). Thus, we operated the following mapping on the data compilation:

$$\begin{cases} x = \dfrac{X_Y^2}{11.42} = \mathrm{Re}_p\sqrt{\tau_*} \\ y = \lambda^* = X_Y Y_Y = \dfrac{\lambda}{D}\mathrm{Re}_p = \dfrac{\lambda u_*}{\nu} \end{cases}, \tag{S6}$$

where $(\mathrm{Re}_p\sqrt{\tau_*}, \lambda^*)$ reflects our new coordinate system. The ordinate λ^* is analogous to a nondimensional wavelength, where the normalization factor is proportional to the thickness of the viscous sublayer, consistent with previous theory (*74-76*). Based on limited data at low values of $\mathrm{Re}_p\sqrt{\tau_*}$, (*25*) hypothesized that λ^* was a constant at low $\mathrm{Re}_p\sqrt{\tau_*}$, i.e., that ripple wavelength was proportional to the thickness of the viscous sublayer. We expanded the parameter space by adding the data of (*24*), which was previously analyzed as analogs to ripples formed by viscous brines on Mars (*26*). The data from (*24*) was extracted from their Tables 5-10 (pp. 124-129). The experiments used silt sizes of about 21 to 115 μm and water-sucrose solutions with kinematic viscosities ranging from $6\text{x}10^{-7}$ to $1.05\text{x}10^{-5}$ m^2/s to explore very small particle Reynolds numbers and thick viscous sublayers.

Figure S7 shows the data of (*24*, *25*) plotted in the new coordinate system, and indicates that dimensionless wavelength, from both datasets, increases with $\mathrm{Re}_p\sqrt{\tau_*}$, inconsistent with the constant dimensionless wavelength hypothesized by (*25*). Because the former study did not distinguish between ripples and dunes, we filtered the sandy bedforms by overlaying the data on the bed stability diagram of (*26*), which itself is a compilation from (*22*, *73*). The bedform stability diagram is a well-accepted phase space that incorporates thousands of observations, and allows one to distinguish ripples from dunes and lower and upper plane bed regimes. The stability diagram

itself can be cast in terms of Re_p and τ_*, which allows the ripples in our data compilation to be segregated from other bed states. The best fit power law relationship to the flume data of (*24*, *25*) for current ripples is

$$\lambda^* = 2450\left(\mathrm{Re}_p \sqrt{\tau_*}\right)^{0.34} \quad (\mathrm{R}^2=0.7414). \tag{S7}$$

The best fit exponent of 0.34 is very close to the rational number 1/3. When the exponent is forced to be equal to 1/3, the best fit relationship to the flume data becomes

$$\lambda^* = 2453\left(\mathrm{Re}_p \sqrt{\tau_*}\right)^{1/3} \quad (\mathrm{R}^2=0.7407). \tag{S8}$$

The relationship in Eq. S8 implies that

$$\lambda = 2453 \frac{\nu^{2/3} D^{1/6}}{(Rg)^{1/6} u_*^{1/3}}. \tag{S9}$$

Equation S9 is in agreement with the predictions of (*1*, *26*, *77-78*) that the wavelength of ripples should scale with kinematic viscosity to the power 2/3. Moreover, most flume experiments suggest that there is a weak correlation between ripple spacing and grain size (e.g., *75*, *79*). Equation S9 also predicts that ripple wavelength decreases with reduced gravity and transport stage—relationships that are in agreement with flume data (*77*).

S4. Paleoatmospheric reconstruction from martian outcrops

S4.1. Technique

The geometry of cross-stratification in sedimentary rocks is a function of the morphology of bedforms, their migration direction, and the rate of net sediment accumulation. In order to anticipate the stratigraphic signature of wind-drag ripples, we employed an algorithm that uses dozens of two-dimensional sine functions to simulate morphology of bedform assemblages, and then moves that evolving morphology through hundreds of steps through time (*30*). To model the martian large ripples, we began with the input values used for Figure 65 of (*30*), changed the superimposed bedforms from dunes to large ripples by reducing their height and wavelength, increased the migration speed of the superimposed large ripples relative to the main dunes as is physically reasonable for smaller bedforms, adjusted the migration direction of the large ripples from directly downslope to obliquely downslope, selected an outcrop orientation through the stratification that most closely reproduced the observed outcrop, and decreased the density of lines in the image to keep them from bleeding together. Results from this modeling exercise suggest that wind-drag ripple cross-stratification would occur in trough cross-sets with preserved foresets bounded by erosional surfaces associated to the wind-drag ripples, themselves bounded by dune-trough scour surfaces.

Theoretical and empirical studies show that subaqueous ripples and dunes, even in the case of zero net deposition, produce cross-sets with thicknesses up to half of the original bedform height, and lengths about half of the original bedform wavelength (*80-82*). Consequently, a 30 cm high wind-drag ripple could produce a ~15 cm thick cross-set if typical subaqueous preservation ratios hold. Transverse eolian dunes typically preserve less than 10% of the total bedform height

(*83*), although this ratio may be much higher for superimposed dunes, up to 100%. In the following, we illustrate how the ripple wavelength scaling relationship can be used to reconstruct the paleo-atmospheric density from measurements of cross-set thicknesses within the Stimson formation at the Apikuni Mountain section at Marias Pass (Fig. S8), Gale crater (Fig. S9).

In order to reconstruct atmospheric density from the thickness of cross-sets, one needs to (i) estimate bedform height from the set thicknesses by assuming a preservation ratio, (ii) estimate bedform wavelength from bedform height, and (iii) solve for atmospheric density based on bedform wavelength using a best fit to our scaling relationship.

In order to place an upper bound on paleo-atmospheric density, we assume a preservation ratio of 100%. Thus, 10-20 cm-thick cross-sets such as those observed at Apikuni Mountain by Curiosity must have been created by the migration of wind-drag ripples with heights of at least ~10-20 cm. Subaqueous and eolian ripples and dunes have height-to-wavelength ratios ranging from ~0.01 to ~0.1 (e.g., *75, 84, 85*). To estimate a conservative upper bound on paleo-atmospheric density, we assume a height-to-wavelength ratio of 0.1, i.e.,

$$\frac{\eta}{\lambda} \approx 0.1, \tag{S10}$$

where η is the ripple height. Thus, the observed cross-sets must to have been created by wind-drag ripples of wavelengths greater than 1 m. Finally, to take into account the scatter associated with measured wavelengths of wind-drag ripple on Mars, we fit the experimental flume data combined with the martian wind-drag ripple measurements. We find the best fit to be

$$\lambda = 2777 \frac{\nu^{2/3} D^{1/6}}{(Rg)^{1/6} u_*^{1/3}} \tag{S11}$$

with a coefficient of determination R^2=0.89, a relationship that is virtually undistinguishable from the best fit relationship resulting from the terrestrial data alone (Eq. S8). The 2777 factor has a 95% confidence interval of 2615 to 2948.

Fig. S10 shows how the predicted wavelength λ of wind-drag ripples from Eq. S11 varies with atmospheric density, and that measured wavelengths of modern large ripples roughly follow the predictions. Fig. S10 was generated assuming a grain size of 200 μm, grain density of 2900 kg/m^3, atmospheric dynamic viscosity of 10.8×10^{-6} Pa.s, gravitational acceleration of 3.78 m/s^2. Bed shear velocity was assumed to be equal to the impact threshold and calculated as a function of atmospheric density following the semi-analytical formulation of (*66*) (all parameter values are summarized in a supplementary ".csv" file). Different atmospheric densities are found under modern conditions due to the wide range in elevation over which bedform-wavelength measurements were made. The ripple measurements of (*27*) were made in the light-toned dusty Tharsis region, while our dataset was acquired over dark mafic sand dune fields. Both datasets show a consistent decrease of ripple wavelength as a function of atmospheric density, but are offset from one another. The offset between the two datasets might arise from: (i) model assumptions that are inexact, e.g., wind shear velocities may not be at the threshold value for transport; (ii) differences in particle size and density, e.g., coarse low-density dust aggregates which may be representative of the bed on the Tharsis Montes (*27*) would form smaller ripples than in mafic sand; (iii) an easier detection of smaller ripples in light-toned material due to a higher contrast between the shadows cast by ripple crests and the bed, such that measurements in dark mafic sands are skewed to slightly larger wavelengths. Most large ripples observed in situ by the Curiosity rover at Gale crater have wavelengths closer to ~ 1.5 meter (Figs. 3 and S10). Bed shear velocities

are likely to be increasingly larger than the impact threshold as atmospheric density increases, an effect that is not taken into account in this formulation. Conversely, while the wavelength of large ripples is expected to increase with elevation, we expect ripples to cease forming at the elevation at which atmospheric density becomes too low to generate winds that surpass the impact threshold. However, large ripples are observed up to the top of Olympus Mons, suggesting that such a threshold in atmospheric density is not reached at the surface of Mars.

S4.2. Cape St. Mary, Victoria crater

The Opportunity rover observed centimeter-scale trough cross-stratification in sandstones of the Burns formation at Eagle and Erebus craters (Fig. 4) (*28, 86, 87*), which were interpreted as the signature of subaqueous ripples in a wet inter-dune environment. The fluvial hypothesis was favored to an eolian origin on the basis of (i) the three-dimensional geometry of the cross-sets, (ii) their scale, and (iii) their paleo-environmental context. These cross-strata are found in sulfate-rich sands of high solubility (*27*), suggesting that shallow subaqueous flows discharged from melt or groundwater as brines of high ionic strength (*26, 37, 38*), rather than sourced from meteoric precipitation under a denser atmosphere. We note that in the absence of additional context (grain size and sedimentary structures like soft-sediment deformation and/or desiccation cracks), the interpretation of the small-scale trough cross-sets is non-unique because they could represent the signature of wind-drag ripples formed in a denser atmosphere. However, independent evidence suggesting wet depositional conditions supports the original interpretation (*86, 87*). In contrast, later along its traverse, the Opportunity rover found ~10-20 cm-thick cross-sets superimposed on high angle foresets on the south face of the Cape St Mary outcrop at Victoria crater (*34*) (Fig. 4). This cross-stratification was interpreted as the signature of out-of-phase sinuous eolian bedforms, stratigraphically above the Endurance and Erebus craters sections; in this location, no evidence of originally wet conditions was observed. The 10-20 cm-thick trough cross-sets of Cape St Mary have the scale and geometry we infer to be representative of wind-drag ripple cross-sets formed under conditions similar to present-day Mars. Martian impact ripples are too small to produce the observed set thicknesses. The observed geometry arises from the migration of smaller bedforms across the lee slope of a larger, host bedform. Coarse-grained ripples migrate slower than adjacent dunes, and their migration would likely not form repeated sets suggesting high deposition rates like those observed in Fig. 4B. Grains have not been directly observed at Victoria crater, but were constrained to be of medium-sand size or finer in other sections of the Burns formation (*28*). Thus, the decimeter-scale trough cross-strata of Cape St. Mary are reasonably interpreted as wind-drag ripple stratification.

The lower bound on the wavelengths of wind-drag ripple we inferred from the thickness of cross-sets at Cape St. Mary in Victoria crater is highlighted with a red dashed line in Fig. S10. Based on our observations, the scaling relationship indicates that the martian atmosphere had a density of $< \sim 0.02$ kg/m^3, and thus overlaps with the range in modern atmospheric densities at the surface of Mars ($\sim$ 0.002-0.023 kg/m^3; gray box). For comparison, under an atmosphere of Earth-like density, wind-drag ripples would have predicted wavelengths of about 12 cm, heights of about 1.2 cm, and thus would form cross-sets < 1.2 cm thick assuming the same preservation and height-to-wavelength ratios.

S4.3. Other candidates wind-drag ripple cross-stratification

Other potential occurrences of wind-drag ripple cross-stratification in the martian geological record were observed by the Mars Exploration Rover Spirit, but were not recognized as such at the time. Decimeter-thick cross-sets were observed as Spirit explored the Home Plate layered plateau in Gusev crater (e.g., *88*). Two interpretations were proposed for the upper Home Plate stratigraphy. A lower unit was thought to be a fallout sedimentary deposit from an explosive volcanic eruption based on its poorly sorted grains, poorly stratified bedding, and the presence of an out-sized clast interpreted as a ballistic volcanic bomb. However, two competing hypotheses were proposed for the upper unit which contains large-scale trough cross-sets of locally well-rounded and well-sorted sand; these were suggested to either result from sand waves associated with the base surge or, alternatively, to be unconformably overlying eolian deposits (*89*). The base-surge interpretation was favored on the basis of a single bedform with a preserved stoss face (*88*). Indeed, the preservation of complete bedforms is rare in the terrestrial eolian rock record (e.g., *83*) owing to generally low aggradation rates of eolian dune deposits. Nevertheless, wind-drag ripples are several orders of magnitude smaller than their host dunes, and by analogy to terrestrial superimposed dunes may aggrade at rates that are high enough to produce steep angles of climb. Textural similarity between the high degree of roundness and sorting of the sandstone grains, and those grains of the modern eolian deposits ("El Dorado") adjacent to the Home Plate outcrop (Figure 6 of (*88*)) further supports the eolian interpretation for the upper unit of the Home Plate stratigraphy.

Candidate wind-drag ripple cross-stratification was also observed by Curiosity at Marias Pass in the Stimson formation (Fig. S8 and S9). There, the observed 10-20 cm set-thicknesses are consistent with a substantially thinned martian atmosphere by the time of Stimson deposition (Fig. S10). The wind-drag ripple interpretation of trough cross-sets at Cape St. Mary is supported by (i) the paleo-environmental context of the outcrop, (ii) the geometry and scale of the cross-sets, and (iii) the coexistence of two distinct scales of cross-sets. In contrast, the candidate cross-strata observed at Home Plate, Gusev crater, and in the Stimson formation at Apikuni Mountain, Gale crater, do not display two distinct scales of cross-sets.

Finally, wind-drag ripples might exist on other planetary bodies in the Solar system, and could be recognized through their distinct morphologies and relatively large sizes on low-atmospheric-density bodies.

Supplementary Figures

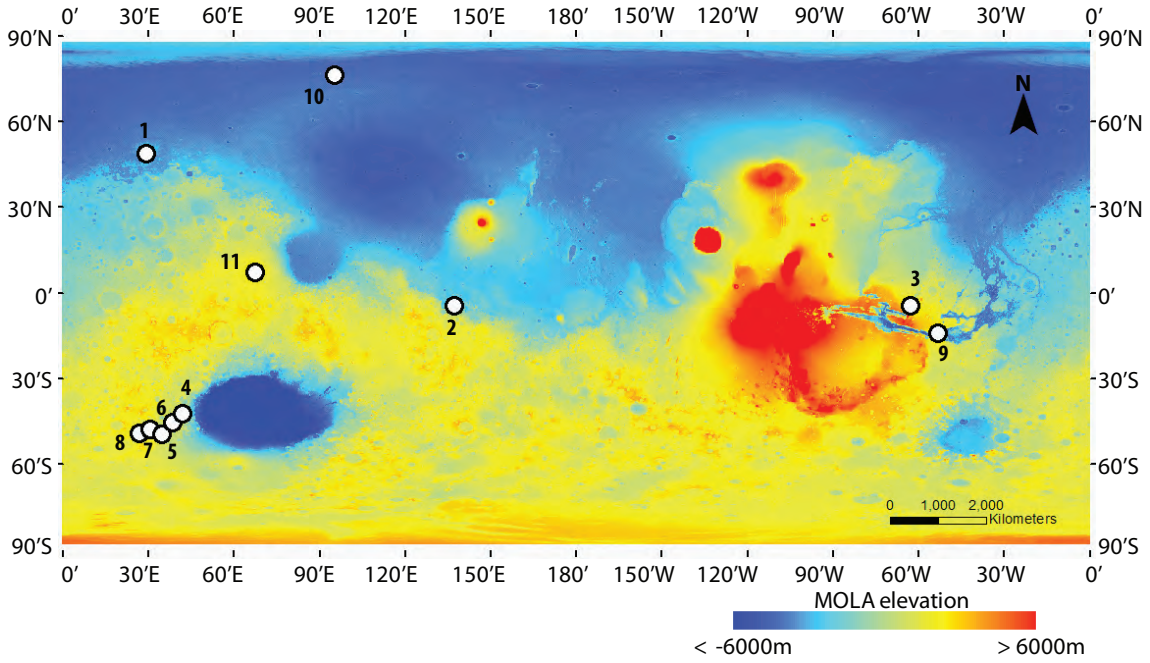

Fig. S1. **Orbital survey of bedform wavelength.** Locations of bedform wavelength measurements overlain on Mars Orbiter Laser Altimeter (MOLA) color-coded topography. Location numbers correspond to those listed in Tables S1 and S2.

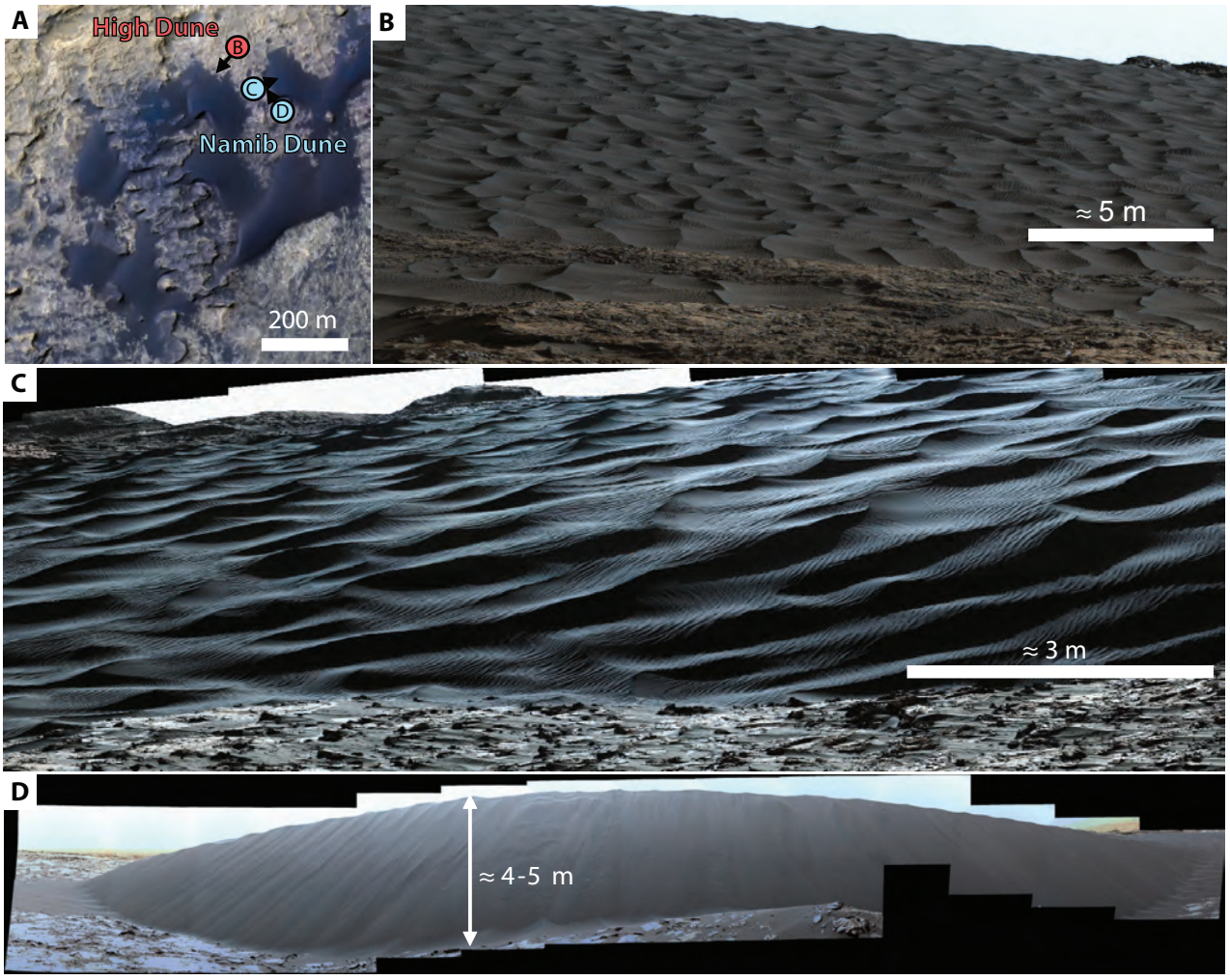

Fig. S2. Bedforms of the Bagnold Dune Field, Gale crater, Mars, near Curiosity's traverse. (**A**) HiRISE context map of the Bagnold Dunes (ESP_035917_1755). Dot-and-arrows show rover location and viewing direction of (**B**) stoss face of High Dune (mcam05301, sol 1169), (**C**) stoss face of Namib Dune (mcam05392, sol 1190), and (**D**) secondary lee face of Namib Dune (mcam05496, sol 1200).

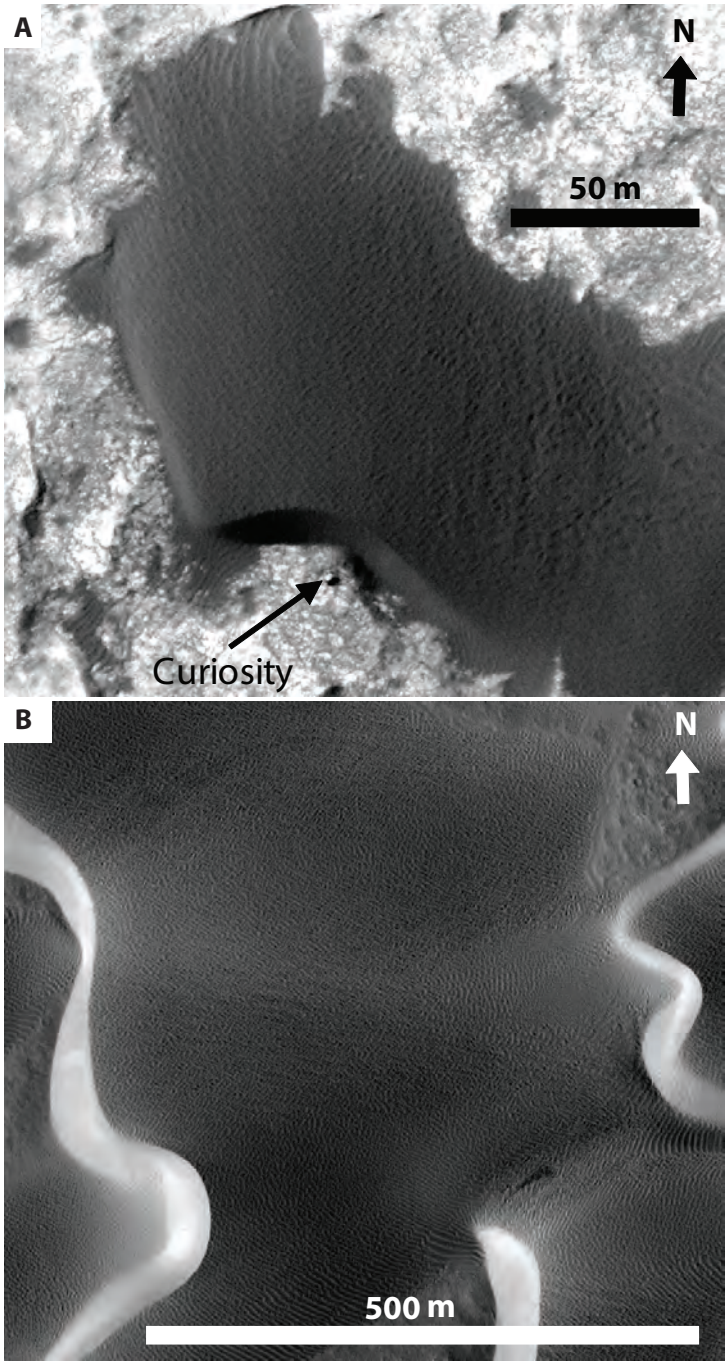

Fig. S3. Curiosity at Namib Dune, Gale crater, Mars. (A) HiRISE image (ESP_044172_1755, 29 Dec. 2015/sol 1207) of Namib Dune, Gale crater. Fig. S2D is a panoramic view from the rover location shown in (A). **(B)** HiRISE image (ESP_038214_1875) of larger dunes at Nili Patera showing that the large ripples do not grow in size up the stoss of their host dune, contrary to compound dunes on Earth (e.g., Fig. S4). Dune in (B) is about the same size as the dune shown in Fig. S4.

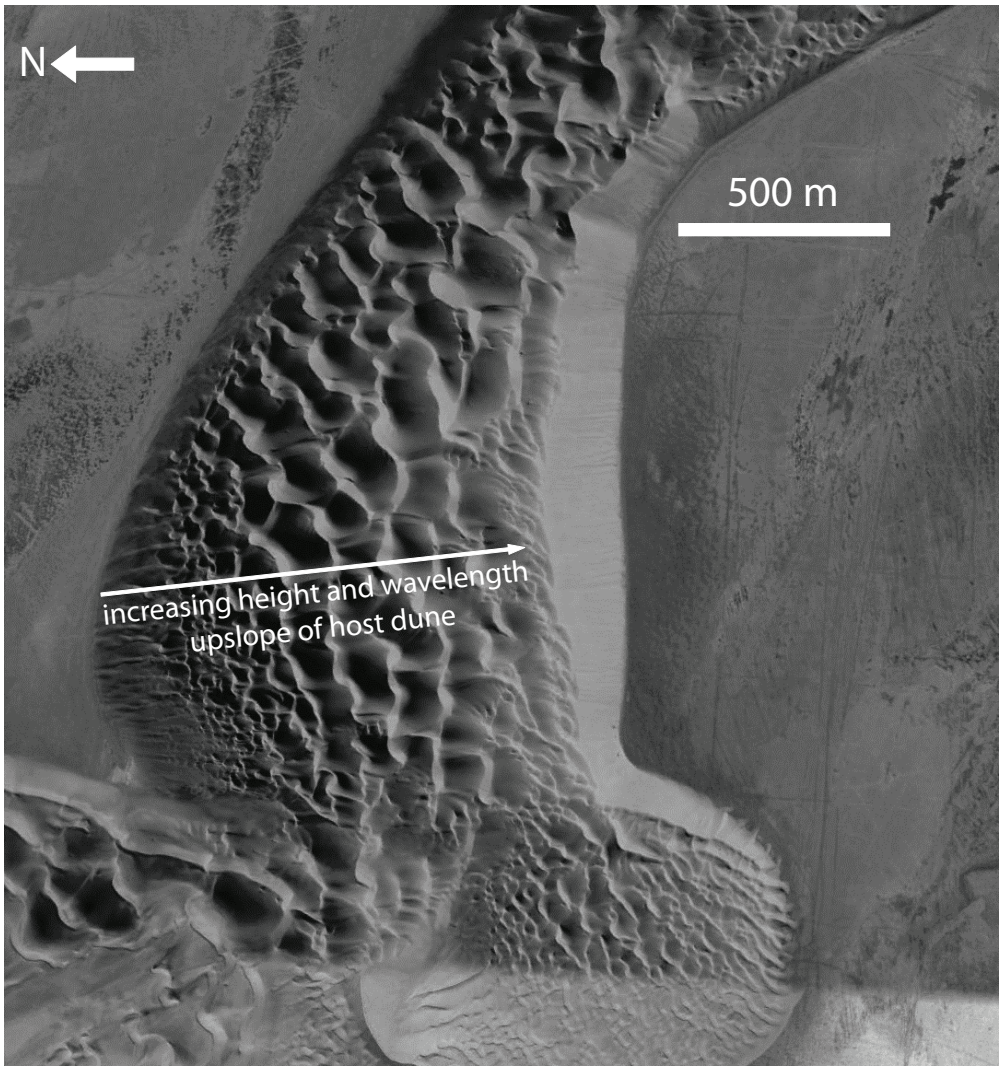

Fig. S4. Compound dunes on Earth. Compound dunes growing upslope of their host dune, Rub'al Khali, Saudi Arabia. Illumination is from the SE (source: Google Earth; 22.298299 N, 54.172680 E).

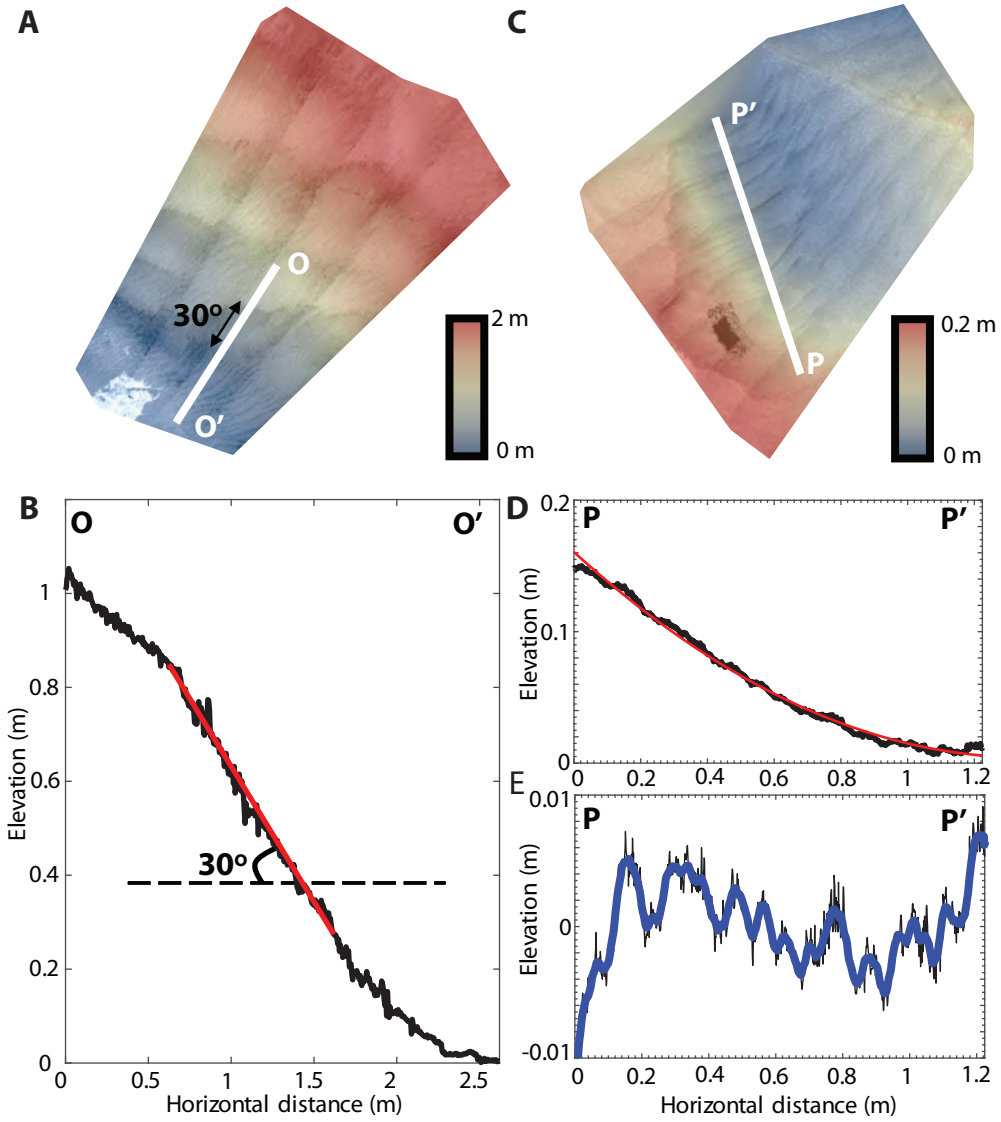

Fig. S5. Rover measurements. (**A**) Digital elevation model (DEM) built from the Mastcam stereo pair mcam05418 (sol 1194) with elevation color-coded. White line indicates location of the profiles shown in (B)**.** (**B**) Topographic profile across a large ripple. Red line represents a linear fit to the angle-of-repose slip face of the large ripple. (**C**) DEM built from the Mastcam stereo pair mcam05372 (sol 1184) with elevation color-coded. White line indicates location of the profiles shown in (D). (**D**) Example topographic profile across small ripples. Red line represents a second order polynomial fit used to calculate (**E**) a corresponding detrended profile. The blue line represents a detrended profile that was smoothed using a 25-point (i.e., 2.5 cm window) moving-average to facilitate bedform identification.

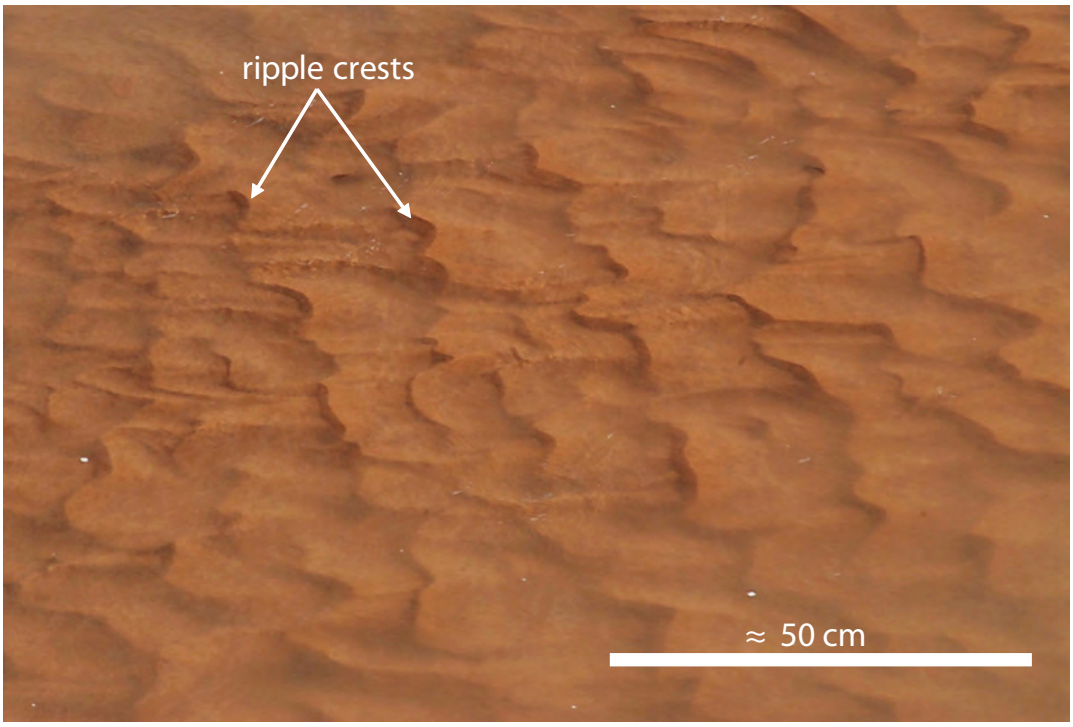

Fig. S6 Current ripples on Earth. Subaqueous ripples in fine-to-medium sand, in a modern stream near the Canyon de Chelly, Arizona, United States (approximately 36.13 N, -109.46 E). Flow is from the top right corner.

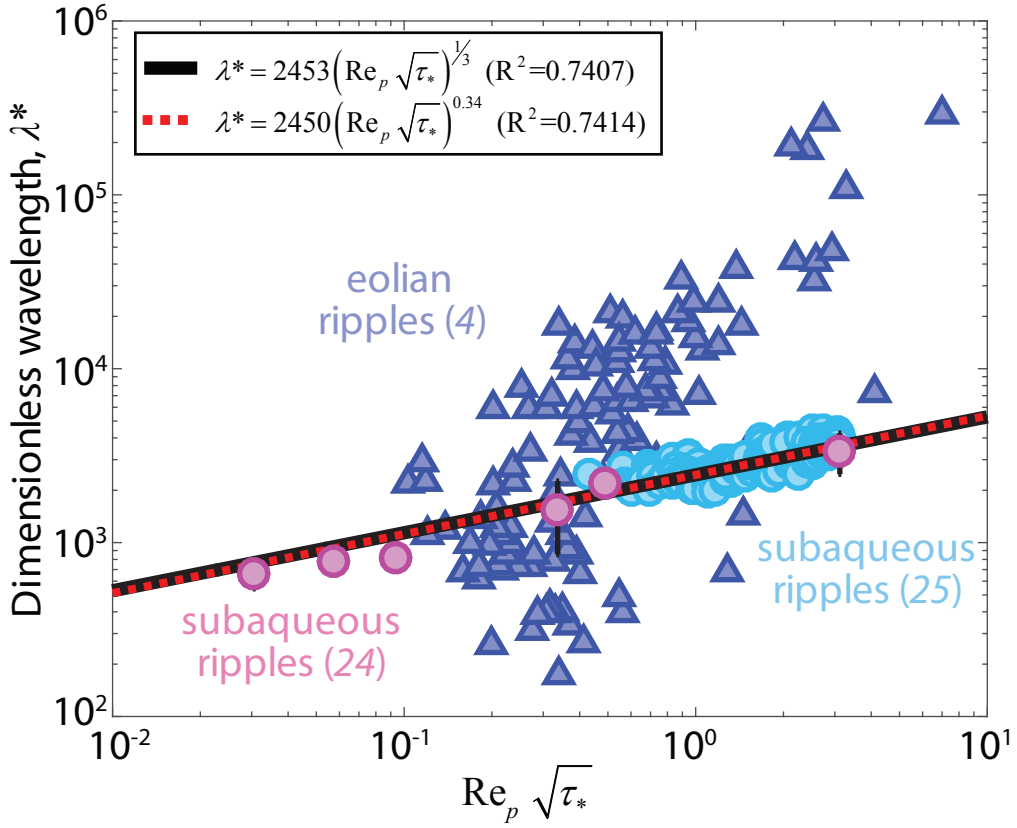

Fig. S7 Fluid-drag theory. Flume data and eolian impact ripples compilation recast in terms of dimensionless wavelength $\lambda^* = \frac{\lambda u_*}{\nu}$ and $\mathrm{Re}_p\sqrt{\tau_*}$ (*4, 24, 25*). The red dashed line is the best fit power law to all current-ripple data of (*24*, *25*). The black line is the best fit power law to all current ripple data of (*24*, *25*) using the rationale exponent of 1/3.

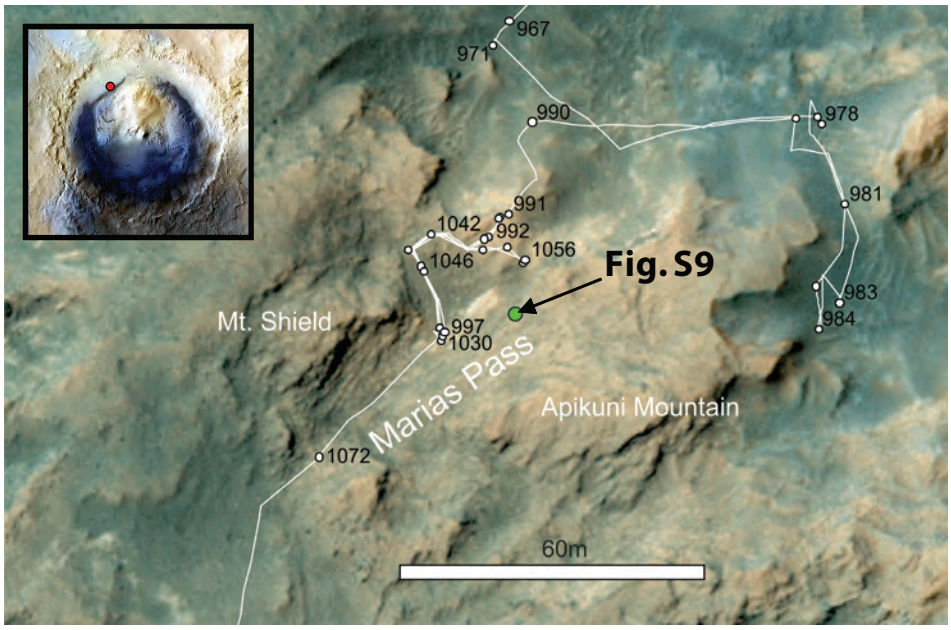

Fig. S8. Location of the Apikuni Mountain outcrop, Gale crater, Mars. Context map (HiRISE color mosaic, location shown in inset; image credit: JPL-Caltech/University of Arizona) with Curiosity rover traverse overlain (white line) near the Apikuni Mountain section at Marias Pass, Gale Crater, Mars. White circles represent rover locations by sol (adjacent numbers). The green dot indicates location of Fig. S9. Gale crater (inset) is about 150-155 km in diameter.

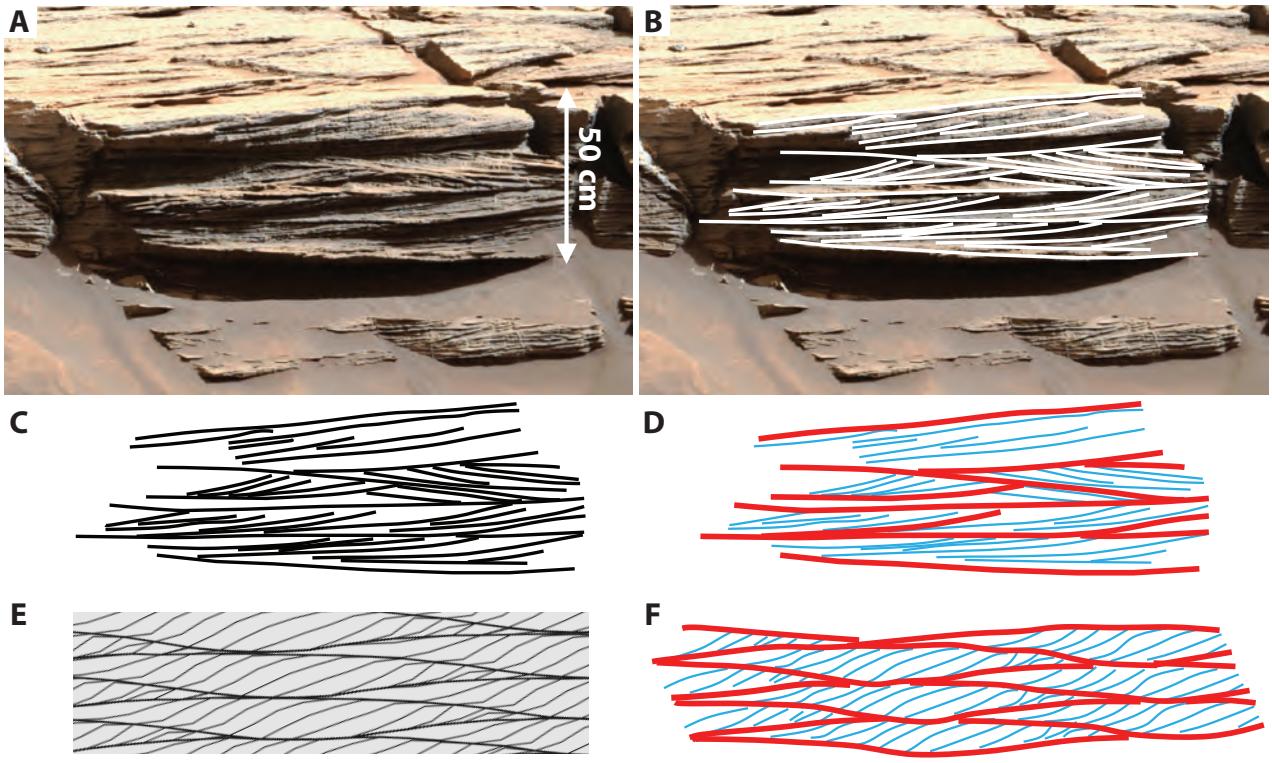

Fig. S9. Trough cross-stratification in the Apikuni Mountain section of the Stimson formation, Gale crater, Mars. (A) Mastcam image (mcam04395, sol 993) of decimeter-scale trough cross-stratification in the Apikuni Mountain section of the Stimson formation, near Marias Pass, Gale Crater. **(B)** Interpretation of cross-set geometry overlain on Mastcam image from (A). **(C)** Uninterpreted stratal features from (B) alone, and **(D)** interpretation of stratal features from (A). **(E)** Sketch of expected preserved stratification produced by wind-drag ripples generated using the algorithm of (*30*), and **(F)** corresponding interpreted stratigraphy. Thick red lines represent erosional surfaces produced by the migration of scours in front of wind-drag ripple lee faces. Thin blue lines indicate wind-drag ripple foreset cross-stratification.

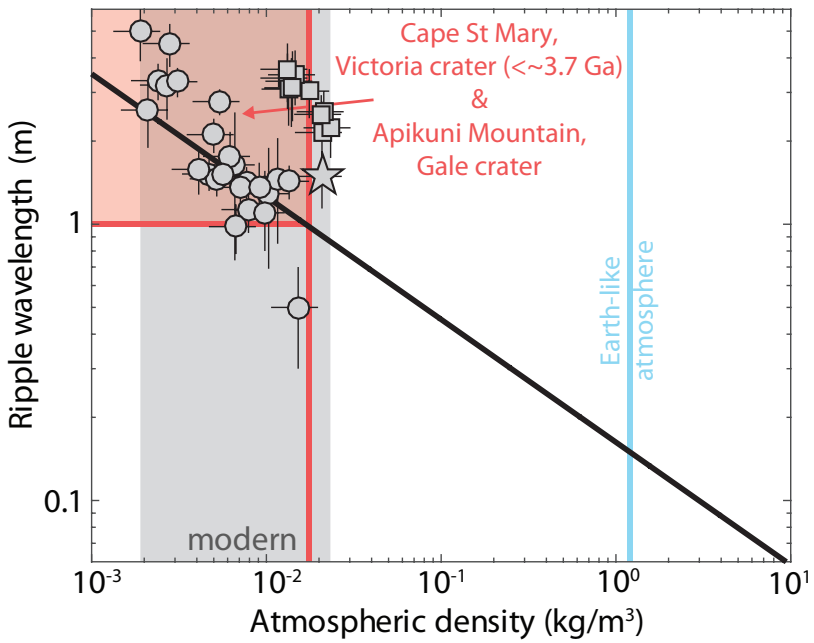

Fig. S10. Wavelength of wind-drag ripples on Mars as a function of atmospheric density. Predicted wavelength of wind-drag ripples as a function of atmospheric density (black line). Gray circles (*27*), squares (this study, orbital) and the star (this study, in situ at Gale crater) represent measured modern large ripples on Mars. Vertical error bars show ± 1^{V} on the wavelength measurements at each given site; horizontal error bars correspond to typical diurnal and seasonal variations in surface atmospheric density of ± 30% the mean value (consistent with measurements at Gale crater, e.g., http://www.jpl.nasa.gov/news/news.php?release=2016-128). The gray box outlines the range in modern atmospheric densities at the surface of Mars, which vary as a function of elevation. The red horizontal line corresponds to the minimum possible ripple wavelength of 1 m inferred from cross-strata at Cape St. Mary in Victoria crater, and Apikuni Mountain in Gale crater; the vertical red line is the corresponding upper bound on paleo-atmospheric density for 1 m wavelength wind-drag ripples.

Supplementary Tables

Area #	Image Name	Latitude (degrees)	Longitude (degrees East)	Elevation (m)	Pixel Scale (cm)	Location
1	ESP_027864_2295	48.905	29.27	-5684.52	30.8	Acidalia Mensa
2	ESP_018854_1755	-4.586	137.392	-4424.172	27.1	Gale crater
3	ESP_034909_1755	-4.5	297.183	-2560.32	26.7	Juventae Chasma
4	ESP_025042_1375	-42.362	42.037	-457.2	25.2	SE of Yaonis Regio
5	ESP_011421_1300	-49.484	34.847	-108.204	25.6	Hellespontus
6	ESP_041987_1340	-45.422	38.83	121.92	25.2	Proctor crater
7	ESP_011909_1320	-47.786	30.689	533.4	50.7	SE of Proctor crater
8	ESP_024502_1305	-49.041	27.224	672.084	50.6	SW of Proctor crater
9	PSP_001970_1655	-14.235	306.735	-4700	26.6	Coprates Chasma
10	ESP_018011_2565	76.182	95.406	-4300	31.7	North Polar erg
11	ESP_039955_1875	7.167	67.751	682.1424	27.9	S of Nili Patera

Table S1. Orbital survey of Martian bedforms: Measurement locations. Location and resolution of analyzed Mars bedforms from HiRISE observations.

Area #	Surface area (km^2)	Dunes		TARs		Ripples		Total number of bedforms
		Wavelength λ (m)	*N*	Wavelength λ (m)	*N*	Wavelength λ (m)	*N*	
1	1.003	131±57	118	5.2±1.8	30	2.2±0.5	116	162
2	0.041	151±67	44	7.0±2.2	33	2.1±0.6	212	168
3	2.210	235±99	60	16.1±7.8	96	3.0±0.6	62	212
4	1.210	199±75	55	8.8±5.6	12	3.5±0.8	130	153
5	1.214	441±264	49	17.8±14.1	80	3.3±0.9	66	159
6	1.229	334±173	31	7.6±3.1	36	3.1±0.9	136	180
7	1.994	573±263	83	10.3±4.0	40	3.1±0.8	138	195
8	1.118	515±189	14	8.3±4.4	40	3.6±0.9	98	141
9	1.504	264±83	31	-	-	2.6±0.5	96	96
10	0.911	248±124	113	-	-	2.5±0.4	104	104
11	1.041	324±111	165	-	-	3.4±0.8	142	181

Table S2. Orbital survey of Martian bedforms: Results. Average measured bedform wavelengths (±1σ). *N* refers to the number of bedforms belonging to each category.

		Mars, orbit		Mars, rover	
		large ripples	**dunes**	**small ripples**	**large ripples**
Earth	**ripples**	3.3×10^{-5}	6.1×10^{-5}	3.1×10^{-2}	1.2×10^{-4}
	dunes	3.3×10^{-5}	2.6×10^{-3}	1.89×10^{-5}	1.2×10^{-4}

Table S3. Statistical analysis of bedform-wavelength distributions. *P*-values of the two-sample Kolmogorov-Smirnov test applied to individual subsampled modes from the three datasets.